FLORIDA STATE UNIVERSITY

COLLEGE OF ARTS AND SCIENCES

GRAVITY AND GEOCHEMICAL CONSTAINTS

ON THE STRUCTURE AND EVOLUTION OF

THE EL VALLE VOLCANO, PANAMÀ

BY

KEITH RICHARD MUNSEY

A Thesis submitted to the
Department of Earth, Ocean, and Atmospheric Sciences
in partial fulfillment of the
requirements for the degree of
Master of Science

2018

Keith Munsey defended this thesis on March 8, 2018.

The members of the supervisory committee were:

David W. Farris

Professor Directing Thesis

James F. Tull

Committee Member

Vincent J.M. Salters

Committee Member

Leroy Odom

Committee Member

The Graduate School has verified and approved the above-named committee members, and certifies that the thesis has been approved in accordance with university requirements.

To my family, Mom, Dad, Matthew & Kyle
To my late grandparents, Harry, Peggy & Antonia whom always supported my academic journey

ACKNOWLEDGMENTS

TABLE OF CONTENTS

LIST OF TABLES

LIST OF FIGURES

ABSTRACT

El Valle is the easternmost volcano in the Central American Volcanic Arc, and is characterized by two periods of volcanic activity, an old group from 10-5 Ma and a young group from 3-0.03 Ma. Both the old and young groups are calc-alkaline in nature. However, the old group is dominantly andesitic, has flat REE patterns, low Sr-Y ratios and contains plagioclase and pyroxene phenocrysts. A subgroup of the older samples also contains biotite. In contrast, the younger group is dominantly dacitic, hornblende-bearing, has low HREE content, high Sr/Y ratios and overall exhibits adakitic characteristics. The transition between the two geochemical groups occurs gradually between 10-3 Ma, at which point the adakitic signature is fully developed. The modern El Valle volcanic edifice is dominated by voluminous young group eruptive products (e.g. the El Hato Ignimbrite) with adakitic-like characteristics.

El Valle is also characterized by a large 40-50 mGal negative Bouguer Gravity anomaly that is apparent in both surficial and satellite gravity measurements. Initial surficial data indicates Bouguer anomalies vary from 40 mGal at the edge of the volcano to -10 mGal in its central caldera. Field lithologic observations paired with the gravity measurements and modeling suggest that the negative gravity anomaly is primarily due to a low-density batholith beneath the volcano.

Samples collected during the gravity survey where geochemically analyzed to distinguish between the various proposed petrogenetic/tectonic models in southern Panamá (e.g. the existence of a slab window, oblique subduction, slab-melting or subduction erosion of Galapagos material). One significant quandary is that geochemical evidence suggests the existence of subduction whereas geophysical data shows a lack of a pronounced Benioff Zone. Modeling suggest that the geochemical signatures can be reproduced via the partial melting of Cretaceous-Early Tertiary lower crustal arc rocks.

CHAPTER 1

GRAVITY AND GEOCHEMICAL CONSTRAINTS ON THE STRUCTURE AND EVOLUTION OF THE EL VALLE VOLCANO, PANAMÁ

1.1 Introduction

The El Valle volcano is one of three recently active volcanoes in Panamá, located in central Panamá on the border of the Coclé and Panamá Oeste Provinces. The volcano is also located at the eastern most extent of the Central American Volcanic Arc. At the summit of the volcano, resides the town of El Valle de Anton, which resides in the 20 km^2 caldera. The volcano experienced two periods of volcanism, the first being dominantly andesitic with a plagioclase pyroxene mineralogy and the second containing mostly dacitic hornblende bearing pyroclastic rocks (e.g. the El Hato ignimbrite) (Defant et al., 1991, 1992; Hidalgo et al., 2011).

Previous geochemistry indicates that the older group volcanic rocks are more enriched in heavy rare earth elements (HREE), with decreasing HREE concentrations, as the samples get younger (Defant et a., 1991). The younger volcanic units are silica rich, have moderate MgO content, high Sr/Y and La/Yb ratios and exhibit an overall adakitic composition. The older andesitic and dacitic units are dated at 10-5 Ma, and are thought to originate by partial melting of the mantle wedge (Defant et al, 1991). To the west, the El Yeguada volcanic center contains andesitic lavas with Old group geochemical signatures up to 15 Ma in age (Defant et al., 1991b). Quaternary volcanic activity resumed at El Valle from ~1.55 to .03 Ma with the eruption of voluminous dacitic pyroclastics (Hidalgo et al., 2011). Defant et al. (1991) suggested that the younger group was derived from slab melting, while Hidaglo et al. (2010) suggested a two-stage process with deep garnet fractionation coupled with mid-crustal amphibole fractionation. The Hidalgo model suggests garnet fractionation occurred at the base of crust coupled with a second mid-crustal stage of amphibole fractionation. The most recent volcanic activity produced the El Hato ignimbrite that blankets the region (56-31 Ka), with a maximum observed thickness of 110 meters (Hidalgo et al., 2010). Previous geochemical investigations show a decrease in HREE concentrations with decreasing age. The conditions which led to the difference in geochemical signatures between the young and old volcanic groups have been a topic of speculation. Overall, the cause is not well constrained. Hypotheses vary from relating to subduction erosion of the

Cocos plate beneath Central America (Goss and Kay 2006), to slab-window processes (Abratis et al. 2001), or to the Caribbean Large Igneous Provence (CLIP) basement involvement. Seismic data suggest that a modern Benioff Zone does not exist beneath the southern boundary of the Panamá Block (e.g. Trenkamp et al. 2002). Alternatively, Rooney et al. (2015) has proposed the occurrence of oblique subduction as being responsible for the adakitic (Young Group) geochemical characteristic.

Constraints on subsurface features beneath the El Valle volcano come either from geochemistry based petrogenetic models mentioned above or from geophysical data sets such as gravity. The primary gravity signature of the El Valle volcano is a broad -30-40 mGal Bouguer anomaly that is observed in both satellite and terrestrial data sets. This project collected over 250 additional gravity measurements around the El Valle volcano in order to better constrain its internal and subsurface structure.

Two hypotheses exist to explain the large negative gravity anomaly: 1) the anomaly is caused by the surficial low-density young group dacitic pyroclastic rocks, or 2) the anomaly is caused by deeper low-density structures beneath the volcano such as a sub-caldera magma chamber or batholith. To determine the cause of the negative gravity anomaly, serial 2.5 dimensional models were produced using the Talwani modeling program (Talwani et al., 1959) to distinguish between these hypotheses. Although it is possible to create models from both hypotheses that fit the data, an unrealistic thickness (several km) of surficial volcanic rocks is required to make the first hypothesis work. Therefore, the model of a large sub-caldera batholith is preferred.

1.2 Geologic Mapping

El Valle has previously been mapped by Defant et al. (1991). Defant's geologic map focuses on the geology around the caldera of the volcano, without mapping the outer flanks of the volcano. In the summer of 2017, field investigations took place at El Valle to collect geophysical and geochemical data, and in the process to construct an updated geologic map. Geophysical data was collected to investigate the low gravity anomaly that characterizes El Valle. Gravity measurements were collected with 1.5-kilometer spacing, radially outward from the center of the volcano, with tighter spacing within the caldera. During the field investigation, rock samples were collected for density measurements and geochemical investigations. In the process of collecting data, observations were made in order to make an updated geologic map .

In addition to previously described units associated with the El Valle volcano, more[a] recently observed volcanics have been added to the map in Figure 1.
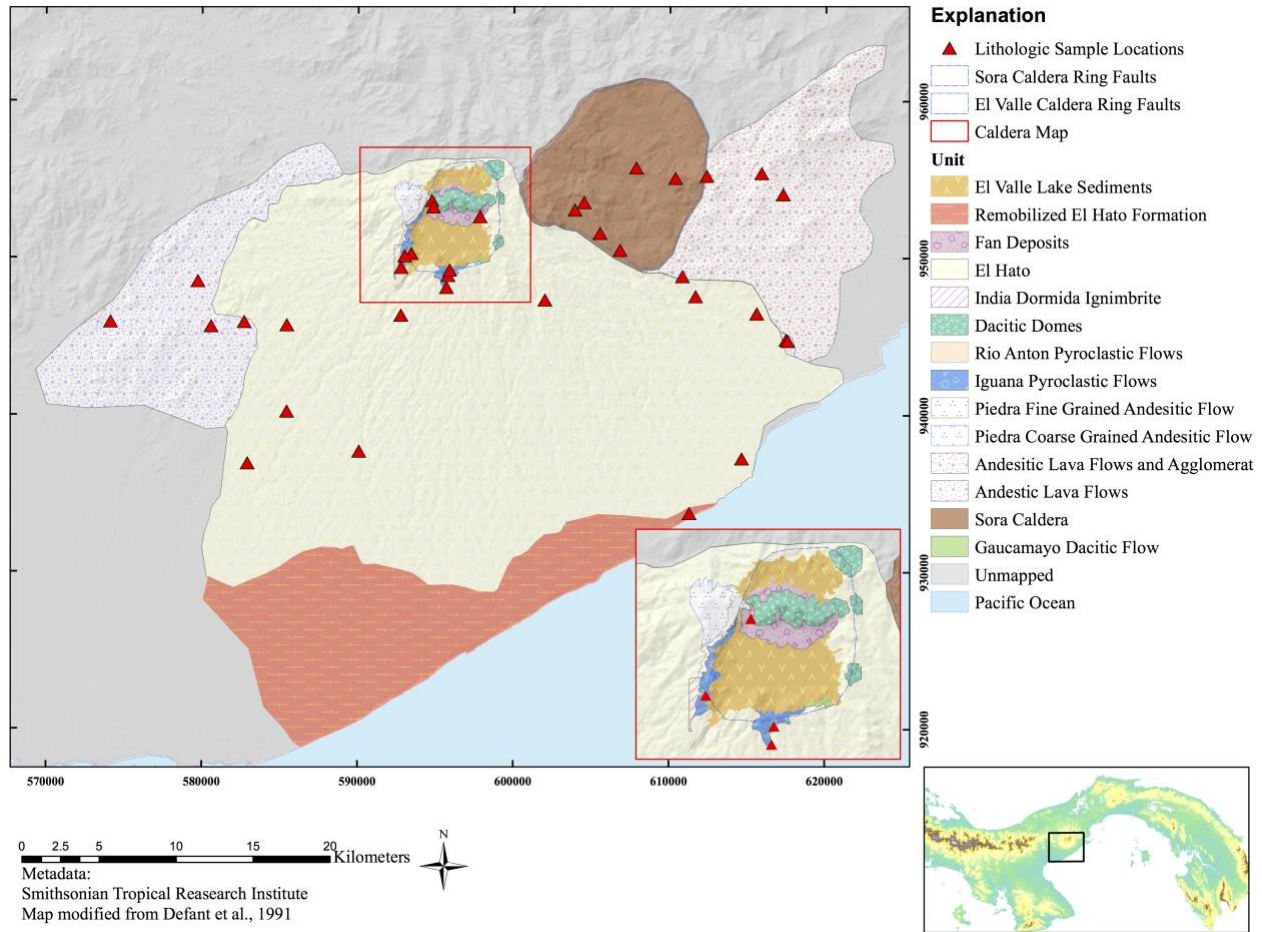
Figure 1: Updated geologic map of the El Valle volcano, Panamá. This map has been modified from Defant et al. (1990); the units have been differentiated based off previous radiometric dating, mineralogy and lithologic observations.

1.3 Geologic Units of El Valle

1.3.1 El Valle Lake Sediments

Lacustrine that were deposited when the El Hato formation settled in in from the caldera walls into the lake that used to be in El Valle.

1.3.2 Remobilized El Hato

Remobilized El Hato can be seen towards to Pacific Coast near El Valle. Sediment transport patterns such as crossbedding can be seen towards the Pacific coast.

1.3.3 Fan Deposits

Dacitic material being deposited in the El Valle caldera as it is being washed out from the Dacitic Domes.

1.3.4 El Hato Ignimbrite

The El Hato is an extensive unit that covers the flanks of the volcano, in particular to the southern portion of the volcano, ranging between dacitic boulders, to lapilli tuff; with primary mineralogy consisting of quartz, plagioclase, hornblende and trace amounts of oxides. The El Hato ranges in thickness and grain size throughout the extent of the unit. Closer to the edifice there are lava clast present in the El Hato, while further away the unit is pumice dominated. El Hato unit erupted about 31.8 Ka (Hidalgo et al. 2011).

1.3.5 India Dormida

This ignimbrite is closely associated with the El Hato Ignimbrite and is dated at 0.22 ± 0.07 Ma.

1.3.6 Dacitic Domes

Three dacitic domes that were emplaced at approximately 1.55 Ma in an east to west lineament across the caldera of El Valle (Defant et al. 1991),with 40% plagioclase, 10% hornblende, 3% quartz and 3% biotite phenocryst.

1.3.7 Rio Anton Pyroclastic Flows

Quaternary pyroclastic lava flows (Defant et al., 1991)

1.3.8 Iguana Pyroclastic Flow

Quaternary dacitic lava flows dominated by plagioclase and amphiboles (Hidalgo et al., 2010)

1.3.9 Piedra Fine Grained Andesites

Fine grained andesitic lavas located on the north-western edge of the edifice and were erupted approximately 6.92 Ma (Defant), with 50% plagioclase, 5% clinopyroxene, 2% oxides (likely iron titanomagnetite) and trace amounts of orthopyroxene phenocryst.

1.3.10 Piedra Coarse Grained Andesites

Coarse grained andesitic lavas located on the north-western edge of the edifice erupted approximately 6.92 Ma (Defant et al., 1991), with 50% plagioclase, 5% clinopyroxene, 2% oxides (likely iron titanomagnetite) and trace amounts of orthopyroxene phenocryst.

1.3.11 Andesitic Lava Flows and Agglomerates

Andesitic lavas with with 50% plagioclase, 5% clinopyroxene, 2% oxides (likely iron titanomagnetite) and trace amounts of orthopyroxene phenocryst. Clast range in size from cobbles to boulder with angular sphericity forming agglomerates mixed in with flows.

1.3.12 Andesitic Lava Flows

Andesitic lavas on the west side of the volcano with 45% plagioclase, 13% biotite, 3% orthopyroxene and trace amounts of clinopyroxene phenocryst.

1.3.13 Sorá Caldera

Andesitic and dacitic lavas and agglomerates with similar mineralogies to previous described units, filling in the topographic depression north east of El Valle de Anton.

1.3.14 Guacamayo Dacitic Flow

Dacitic lava flow with K/Ar ages of 10.19 ± 0.37 Ma.

CHAPTER 2

GRAVITY INVESTIGATION ON THE SURFICIAL AND SUBSURFICAL STRUCTURE OF THE EL VALLE, VOLCANO

2.1 Abstract

The El Valle volcano is the easternmost volcano of the Central American Volcanic Arc and is characterized by two periods of volcanic activity. The older volcanic rocks are predominantly andesitic, while the younger group is composed of dacitic flows and pyroclastic units, including the most recently erupted El Hato ignimbrite that blankets the region around the volcano. El Valle is also characterized by a large 40-50 mGal negative Bouguer Gravity anomaly that is apparent in both surficial and satellite gravity measurements. Terrestrial gravity data indicates Bouguer anomalies vary from 40 mGal at the edge of the volcano to -10 mGal in the central caldera. Field lithologic observations paired with the gravity measurements suggest that the negative gravity anomaly is caused by low-density young group dacitic pyroclastic rocks and the most recently erupted El Hato ignimbrite, in conjunction with a large sub-caldera intrusive body. Quantitative 2.5-dimensional modeling was done to investigate the influence an intrusive body and low-density surficial volcanics would have on the gravity signature observed in and around the El Valle volcano. Results from the modeling strongly indicate that a large sub-caldera plutonic body exists beneath the El Valle volcano and the adjacent caldera systems.
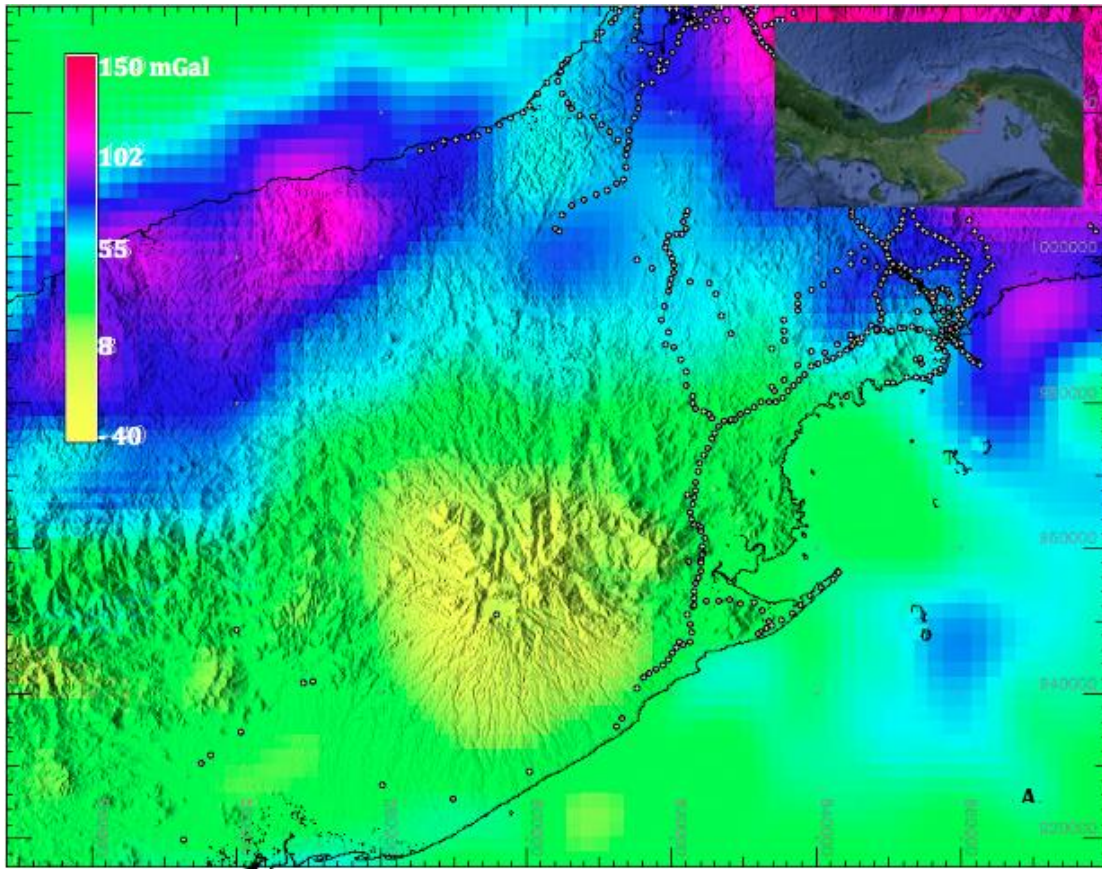
Figure 2: Regional Bouguer gravity map calculated from Sandwell and Smith (2009) satellite free-air gravity data indicating that the region of El Valle exhibits a large low gravity anomaly (represented in yellow).

2.2 Geologic History

2.2.1 Tectonic Setting of Panamá

The region that encompasses Panamá is one of the most complex tectonic environments in the world, due to the interactions between the Panamá block, and the Caribbean, South American, Cocos and Nazca plates (Figure 2). The Panamá Arc initially formed on the on the western margin of the Caribbean Plate due to the subduction of the Farallon Plate at approximately 73 Ma (Buchs et. al. 2010), as illustrated in Figure 3. Buchs et al. has found 73 Ma basaltic dikes in the Azuero Peninsula exhibiting subduction related signatures, giving an estimate as to the age of arc initiation. Wegner et al., 2011, defined three main episodes of arc volcanism in Panamá: 1) an initial Late Cretaceous through Eocene arc, 2) an enriched Miocene Arc primarily active in western Panamá, and 3) Pleistocene and younger adakitic like magmatism also present in western Panamá. Farris et al., 2011 and 2017 also note an episode of extensional volcanism localized within the Panamá Canal basin.
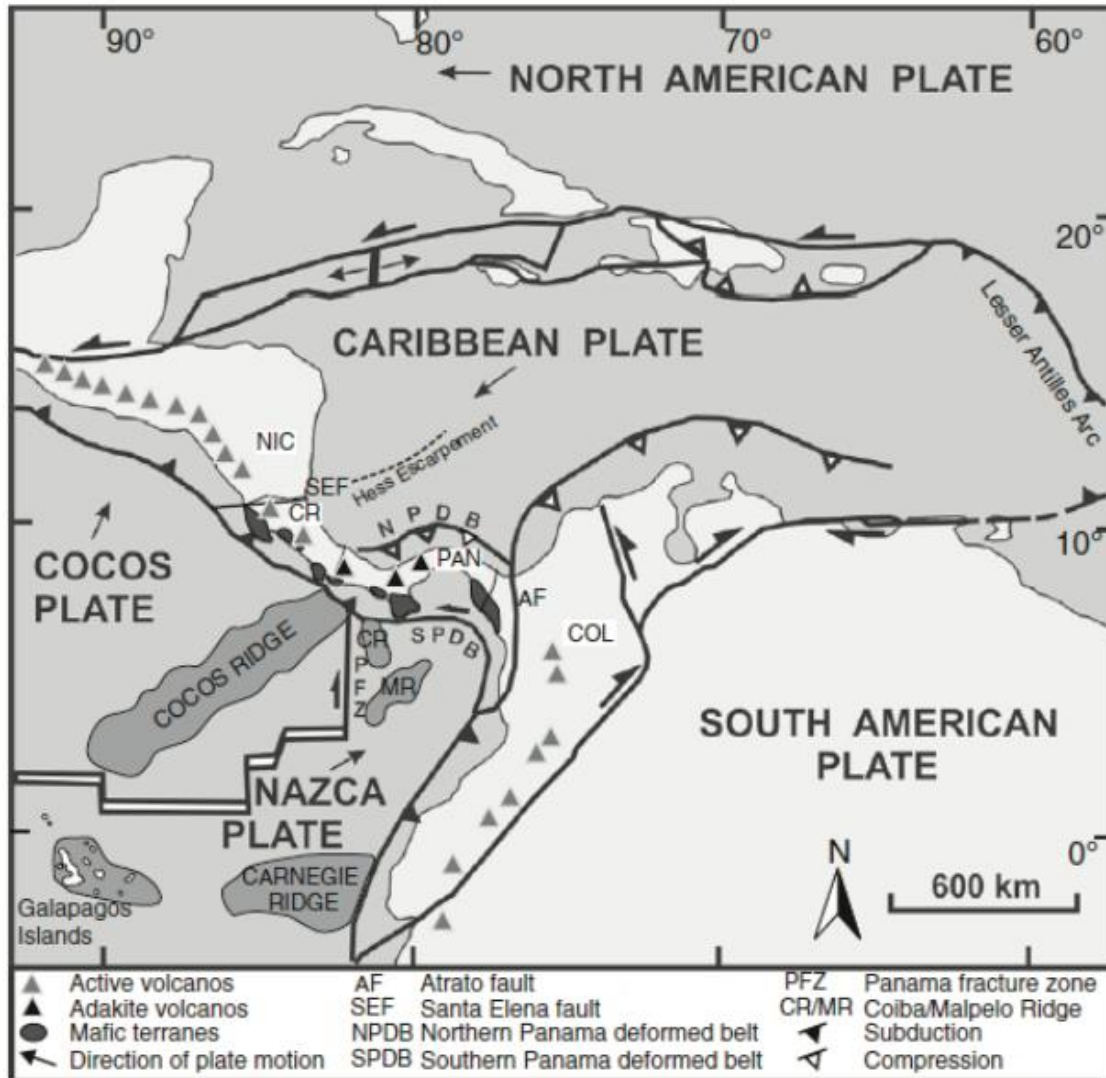
Figure 3: Tectonic map of the Caribbean illustrating, plates, plate motions, major faults and volcanic terrains; from Meschede and Frisch, 1998.

During the Late Campanian to Middle Eocene, the southern convergent margin of the isthmus was also affected by right-lateral transpressive deformations (Corral et al., 2013), seamount (Wegner et al. 2011) accretions (Buchs et al., 2011a,b), and subduction erosion, as witnessed by detailed biochronology, igneous and sedimentary geochemistry, and tectonostratigraphy in the fore-arc regions of the Nicoya, Osa and Azuero Peninsulas (Bandini et al., 2008; Baumgartner et al., 2008; Baumgartner-Mora et al., 2008; Buchs et al., 2010, 2011a). During the Middle Eocene, arc volcanism terminated in eastern Panamá (Lissina, 2005; Montes et al., 2012b; Wegner et al., 2011). Regional uplift of the volcanic arc occurred during the Eocene based on apatite fission track and U/He dating (Farris et al. (2011), Montes et al. (2012a). Paleomagnetic data collected by Montes et al. (2012b) indicates the volcanic arc in central Panamá was ~100 km offset by left- lateral strike-slip motion between 38 Ma and 28 Ma after fragmentation, which resulted in counter clockwise block rotation. This rotation increased around 28 to 25 Ma leading to northward displacement of the volcanic arc. This rotation was followed by
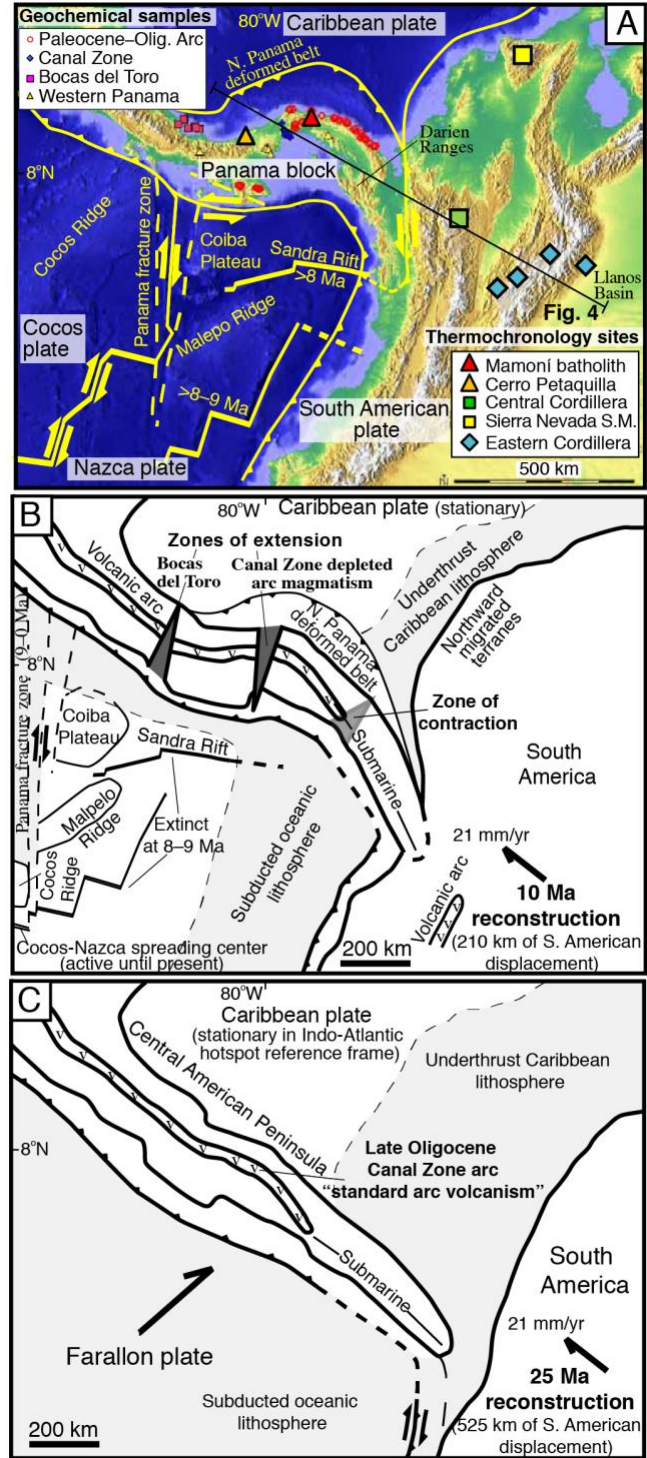
Figure 4: A) Modern tectonic map of Panamá with the locations of previous geochemical samples. B) Tectonic reconstruction at 10 Ma during the collision of South America and Panamá. Here there are two zones of extension (Bocos del Toro, Canal Zone) and one zone of contraction in eastern Panamá. C) Reconstruction at 25 Ma, after the collision of Panamá and South America. Caribbean Crust was thrust beneath South America. (Farris et al. 2011)

subsidence that resulted in the formations of multiple basins in Panamá (Coates et. al. 2004).

During the Late Oligocene (25 to 23 Ma), the Farallon Plate broke up into the Cocos and Nazca Plates (Figure 4). This event had important consequences for the tectonic and volcanic conditions of the area such as change of direction and increased spreading rates along the East Pacific Rise (Goff and Cochran 1996) and faster less oblique subduction at the western margins of the Central American trenches (Sempere et al. 1990). Subduction under the Caribbean plate created the Central American Arc, which contains hundreds of volcanoes and spans 1500 kilometers. The extent of the Central American Volcanic Arc in Panamá consists of ten major stratovolcanoes. Beneath modern Panamá there is a lack of a well-defined Benioff zone along its southern margin, which is due to either subduction of young hot oceanic lithosphere (de Boer et al 1988) or detachment of the subducted slab. Slab detachment may have occurred at 5-10 Ma, coinciding with the cessation of spreading at the Sandra Rift (Lonsdale, 2005). The changes in volcanic activity and arc uplift around 24 Ma could be related to the breakup of the Farallon Plate and/or the increased westward motion of the South American plate in relation to the Central American Plate (Farris et al. 2011). A range of evidence, such as arc geochemical changes, broad exhumation of the northern Andes and Panamá, as well as extensive foreland deposition in the distal Llanos Basin of Columbia suggest that the collision initiated between 23 and 25 Ma when South America impinged upon Panamá arc crust (Farris et al., 2011). Geochemical data as well as tectonic reconstructions suggest that the Panamá block underwent arc-perpendicular extension, possibly during the formation of the Panamá orocline (Silver et al., 1990). Farris et al. (2011) suggests that there are two zones of extensional magmatism at the Canal Zone and Bocos del Toro (Figure 4) and one zone of contraction in the Darien Ranges.

The subduction of various plates led to the generation of the Panamá arc; however eventually, northward subduction came to an end. Evidence of subduction termination can be seen in the linear magnetic anomalies of the Sandra Rift which lies south of Panamá, which suggest northward spreading of the rift terminated at approximately 8 Ma (Lonsdale et al. 2006). In addition, the end of spreading along the Sandra Rift is synchronous with the formation of the Panamá Fracture zone. Linear magnetic anomalies and lack of a Benioff zone suggest an absence of subduction, however modern volcanism exhibit subduction related geochemical signatures. Rooney et al. (2015) attempted to accommodate this problem by suggesting the onset of oblique subduction after the cessation of Sandra rift activity (8 Ma). Modern volcanism in Panamá also

contains adakitic characteristics (e.g. high Sr/Y and La/Yb ratios) that were interpreted by initial workers as resulting from slab melting. This signature is present is volcanic rocks younger than 3-4 Ma, and some characteristics occur in rocks as old as 8-10 Ma, suggesting that it may be related to the end of northward subduction.

Overall, Panamá arc magmatism initiated at 73 Ma, with the subduction of the Farallon Plate beneath the Caribbean Plateau. Initial arc volcanic rocks are hydrous, relatively depleted in REE, but have a larger Nb-Ta anomaly indicating strong fluid flux from the slab into the mantle wedge. Between 30 to 40 Ma there was a hiatus of magmatic activity with resumption of arc volcanism by 25-30 Ma. Geochemical and geophysical data indicate that the western Canal basin volcanic rocks formed due to the influx of young juvenile mantle in an extensional tectonic setting. One proposed explanation is the existence of tear in the subducted slab due to the ongoing collision of Panamá and South America. This is consistent with the fracturing of the Isthmus as proposed by Farris et al. (2011), and a tear in the underlying slab would allow for the influx of young mantle material. The Miocene El Valle volcanics that make up the Old Group lie along the transition between the extensional volcanics to the east, and the depleted REE western Panamá rocks. The younger Miocene arc magmatism is characterized by lower REE values and higher concentrations of LILEs (Wegner et al., 2011). The youngest episode of volcanism in Panamá occurring after 3-4 Ma, ranges in age from 1.3Ma till recent and contains an adakitic signature with elevated Sr/Y ratios steep REE patterns with strongly depleted HREE and moderate MgO content.

Figure 5:
A) Young Group Volcanics are dominated by dacitic lavas and tuffs, located along the rim of the caldera and on the flanks of the volcano. Primary mineralogy consists of quartz, plagioclase and biotite. Densities of rocks within this unit are lower than the old group.

B) Columnar jointing found in the old group volcanics underlying the El Hato Ignimbrite. Mineralogy consist of pyroxene and plagioclase.

C)El Hato Ignimbrite that covers the flanks of the volcano, with exception of the northern region. Mineralogy consist of quartz, plagioclase and hornblende, with clast ranging in size, with larger clast closer to the edifice.

2.2.2 Geology of El Valle Volcano

The El Valle volcano, located in Central Panamá, is the easternmost volcano in the Central American Arc (Figure 1). The base of the volcano is blanketed with Quaternary ignimbrite deposits that extend southward from the volcano caldera towards the Pacific coastline (the El Hato Ignimbrite). At the summit, there is a 20 km^2 caldera where the town of El Valle de Anton is located. The oldest eruptive unit exposed within the caldera is the Guacamayo Dacitic Flow, which has a K-Ar age of 10.19 ± 0.37 Ma (Defant et al., 1991).

Other early (Old Group) eruptive units include the Piedra Fine Grained Andesites, the Piedra Coarse Grained Andesite (K-Ar age of 6.92 ± 0.53 Ma), the Llano Tigre (Ar-Ar age of

5.14 ± 0.34 Ma) and the Rio Anton, and Iguana Pyroclastics (Defant 1991a, Hidalgo et al, 2011). A 3.5 Ma period of quiescence followed the eruption of the Llano Tigre Andesites, which ended about 1.55 ± 0.25 Ma with the emplacement of a dacitic dome that overlooks the El Valle Caldera. Shortly after, at approximately 1.33 Ma, the eruption of the extensive El Hato Ignimbrite occurred covering the flanks of the volcano, specifically the to the south of the edifice. This eruption likely caused formation of the modern El Valle Caldera followed by the continued eruption of east-west orientated dacitic domes from 0.9-0.2 Ma (Defant 1991a). The youngest reported volcanic activity at El Valle comes from Hidalgo et al. (2011) who reports Ar/Ar ages as young as 32 ± 0.27 Ka. These younger group units are dominantly dacitic, hornblende bearing, have low HREE values, and high Sr/Y ratios. Following the collapse of the El Valle caldera, El Hato sediment was reworked and deposited as the El Valle formation, a lacustrine deposit reaching more than 90 meters of thickness inside the caldera (Defant et al., 1990). The contrasting lithologies of the Old and Young Group volcanics cause density differences that can be utilized in gravity modeling (Figure 5).

2.3 Methods

2.3.1 Geologic Mapping and Rock Sampling

In the July of 2016, rock samples were collected from the various rock units associated with the El Valle volcano. Sample locations are plotted in Figure 1, and samples were collected to perform geochemical analyses, lithologic descriptions and density measurements. Densities were calculated by measuring the mass of displaced water when submerged (equal to the volume of displaced water), the mass of the dry sample, and dividing the dry mass by the volume. These measurements were carried out at least three times, averaged and are estimated to have a precision of 0.05 g/cm^3. These measurements were collected to provide constraints on the gravity models.

2.3.2 Gravity Data Collection

Previous El Valle gravity data include 1) several ground based points from the Bureau Gravimetric International (BGI) database and satellite based observations (Fig. 2). Both suggested a broad regional Bouguer gravity low of 40-50 mGal centered on the El Valle volcano. It is apparent from Sandwell and Smith (2011) satellite gravity data that El Valle is characterized by a large regional low gravity signal seen in Figure 2. At the beginning of this study, the low

gravity signal was originally theorized to be due to the expansive, low density El Hato Ignimbrite.
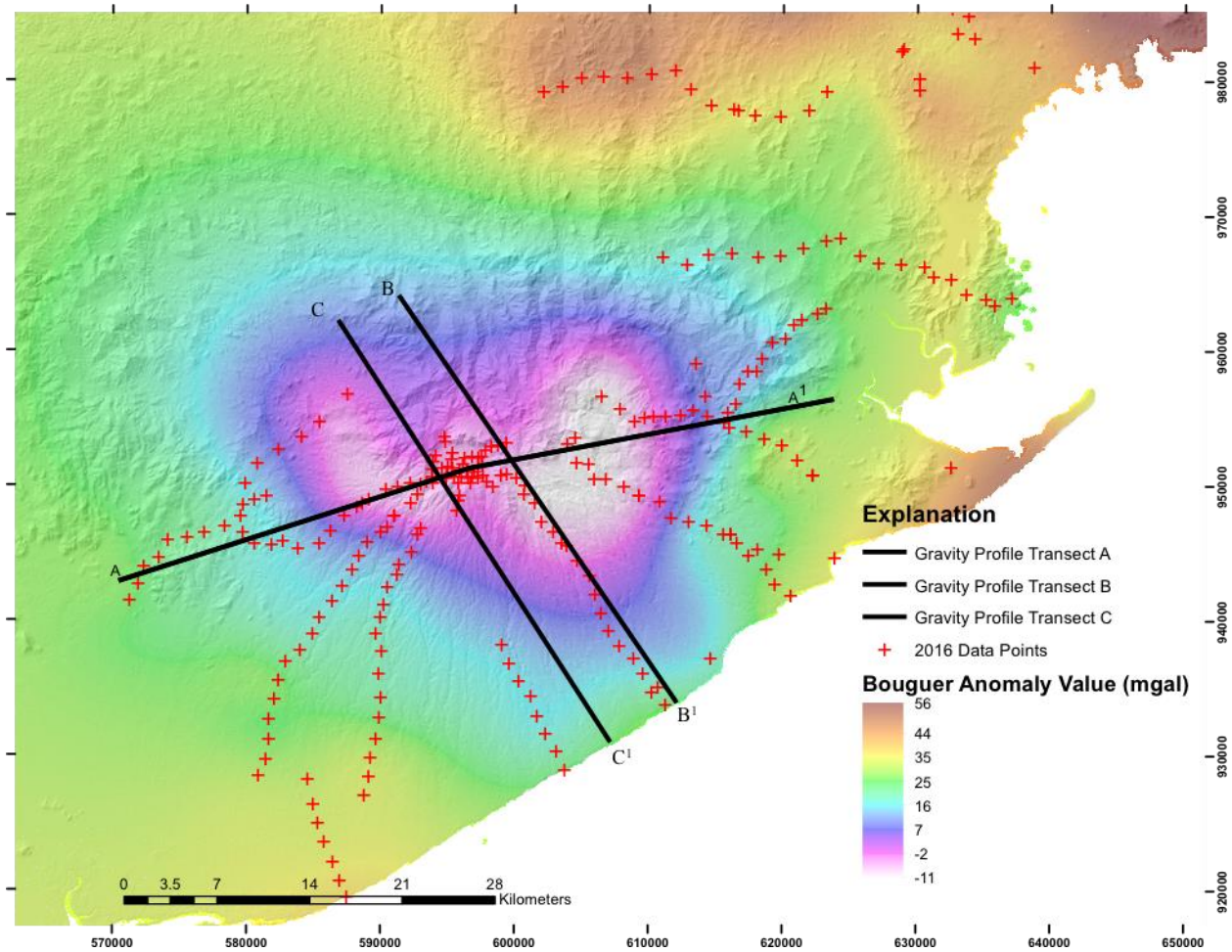
Figure 6: Bouguer anomaly map generated using interpolated surficial gravity data that was collected and corrected in the summer of 2016. Data points are represented by the red crosses; the transect lines correspond to the gravity models that can be seen in Figures 7-10.

During the summer of 2016, 275 gravity measurements were collected in the vicinity of the El Valle volcano, with a higher density of data points inside of the main edifice of the volcano. Gravity data was collected using a Worden gravimeter, which uses a zero length quartz spring within a vacuum tube. When leveled, a dial reading can be acquired and then converted into a relative or absolute gravity value in mGals via reference to previously measured gravity stations. The conversion from dial units to mGals is done using the dial constant of 0.08044 mGal/dial constant. The instrument has a sensitivity of 0.01 mGal and a measurement reproducibility of 0.1-0.2 mGal. During each day of gravity measurements, a local base station was reoccupied at the beginning and end of each collection day, to correct for variables such as

14

earth tides and instrument drift. Finally, all local gravity measurements in this study were tied into an absolute value (978,228.998 mGal, D'Agostino et al., 2010) at the Instituto Geográfico Nacional Tommy Guardia in Panamá City, Panamá.

At El Valle, gravity measurements were taken in a series of radial transects around volcano with approximately 1.5-kilometer station spacing. The distribution of gravity points on the flanks of the volcano was limited mainly by the road system. Within the caldera, gridded gravity measurements were taken at .3 to .5-kilometer spacing. Elevation measurements were acquired using a Trimble ProXRT differential GPS, providing differentially corrected elevations accurate to within 10-50 centimeters; this accuracy is necessary due to gravity being affected by elevation. The Trimble GPS was used to collect an average of 300 GPS measurements per station, which were then differentially corrected in order to collect an accurate location and elevation.

2.3.3 Latitude, Free Air and Bouguer Corrections

Standard gravity corrections of latitude (a.), free air anomaly (b.), and simple Bouguer anomaly (c.), as described by Blakely (1995), are used to compensate for the affect the Earth's shape and rotation, and elevation and crustal mass above sea level, respectively on gravitational observations. The latitude correction is applied to the gravity measurements to compensate for the elliptical shape of the Earth and its rotation; this is due to gravitational acceleration being influenced by the distance from the observation point from the center of the earth as well as the Earth's rotation. This gravitational effect is calculated for using the latitude correction. The free-air correction is utilized to compensate for the decrease in gravitational force due to the increasing distance from sea level at the location of a surveying site. The simple Bouguer correction compensates for the mass of material located between the surveying location and sea level and uses a slab to approximate topography. These calculated values are then used to calculated a Free Air Anomaly (d.) and a Simple Bouguer Anomaly (e.), the latter of which is used in the various modeling techniques used in the study. Terrain corrections were spot checked and found to be less than 1-2 mGal for most stations.

a.

$$G_0 = 9.7803267714 \cdot \left[\frac{1 + 0.00193185138639 \sin^2 \lambda}{\sqrt{1 - 0.0066943799013 \sin^2 \lambda}}\right]$$

b.

$$g_f = h \cdot 0.3086$$

c.

$$g_B = 2\pi\rho h$$

d.

$$Free\ Air\ Anomaly = Gravity_{abs} - Gravity_0 + g_f$$

e.

$$Bouguer\ Anomaly = Free\ Air\ Anomaly - g_B$$

2.3.4 Gravity Modeling

The corrected data is used to produce gridded Bouguer anomaly maps, from which profile data can be extracted and used to produce gravity model transects. The GRASS GIS program was used to grid the data (Grass Development Team, 2017). The gravity models were generated in Talawani (Talwani et al., 1959). The Talwani modeling program generates 2.5-dimensional models using the technique of Talwani et al. (1959) and Cady (1980). Bouguer anomaly transect data is imported into the Talwani program along with dimensional measurements and densities to produce these models. 2.5 dimensional models allow for an extra parameter accounting for "strike in, strike out" to be applied to the model unlike 2-dimensional modeling programs. This allows for gravity models to account for some 3-dimensional variation and differentiate between geologic units that are not well approximated by infinite 2-D prisms and those that are more equant in shape such as small basins, caldera fill material and plutons.
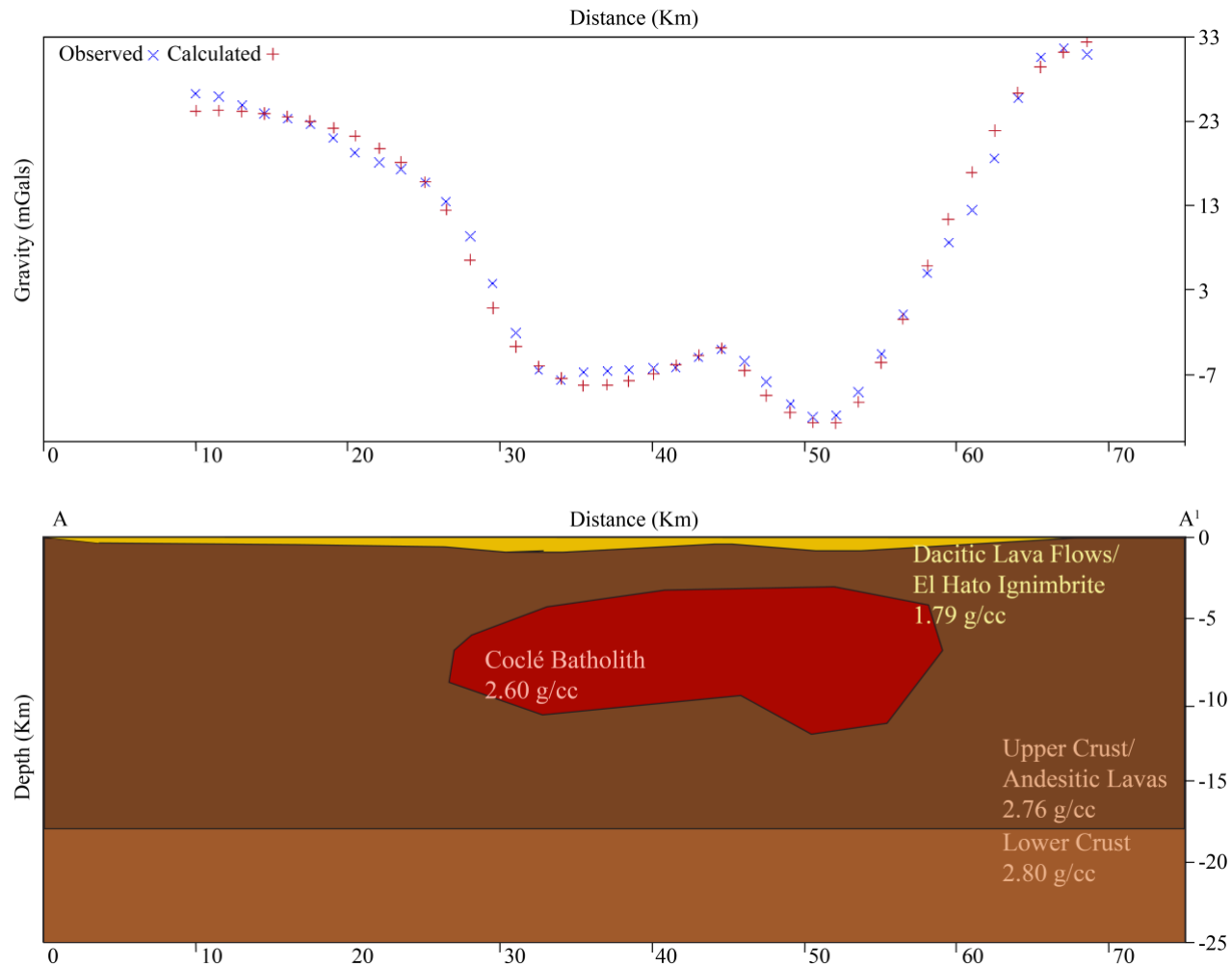
Figure 7: Gravity Model A, produced using Talwani. Transects A to A1, running west to east across the volcano and through the El Valle caldera. The model suggests two centers where there is a thickening of dacitic lavas/El Hato ignimbrite occurs, these areas correspond to the El Valle and Sorá calderas (respectively, from west to east).

17
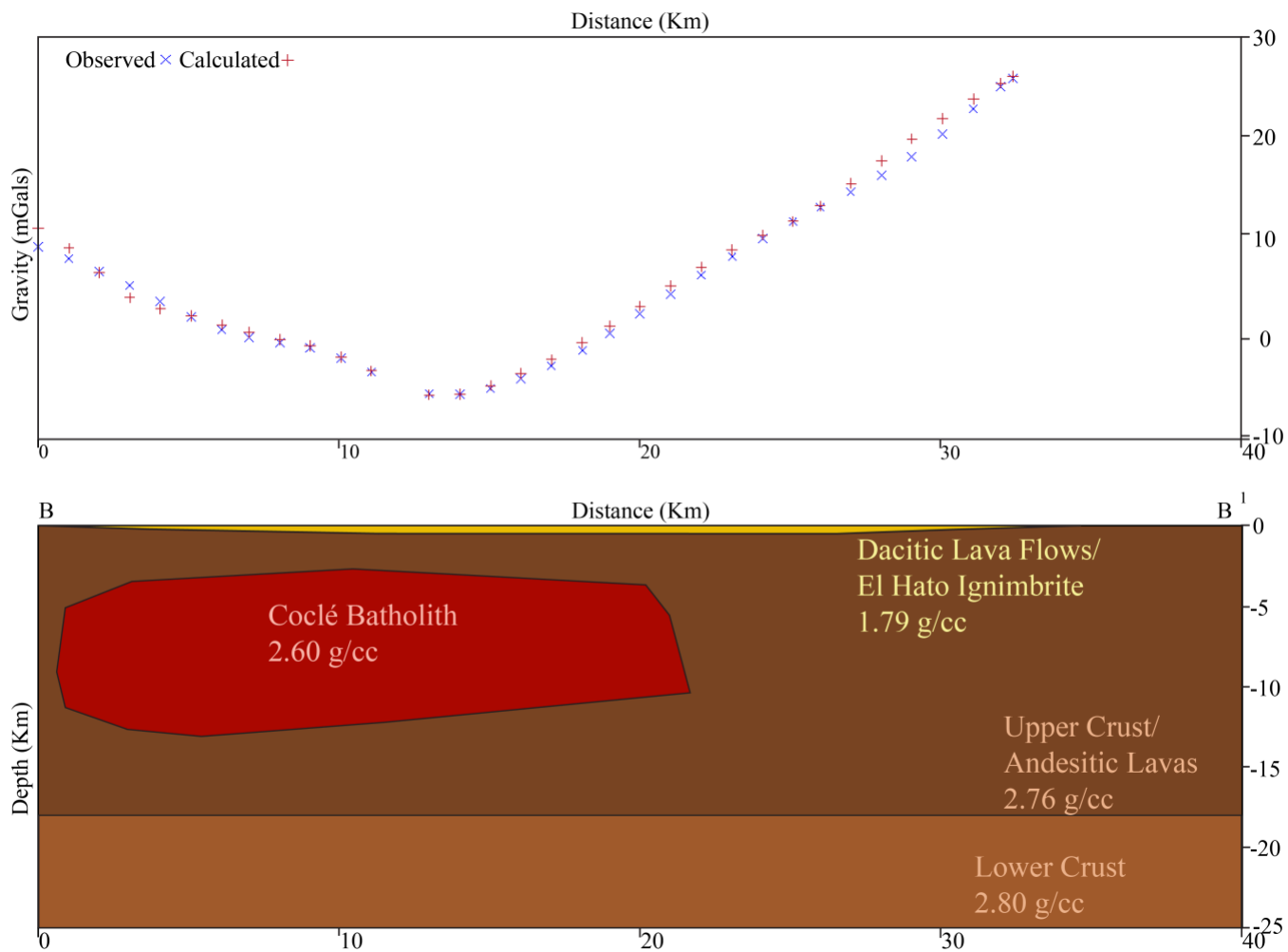
Figure 8: Gravity Model B, produced using Talwani. Transects B to B1, running north to south across the volcano. Dacitic lavas/El Hato Ignimbrite thin towards the coast, and are not present north of the El Valle caldera. The lack of a strong low gravity anomaly north of the transect line could be an artifact of a batholith and dacitic lavas/El Hato missing north of the El Valle caldera.
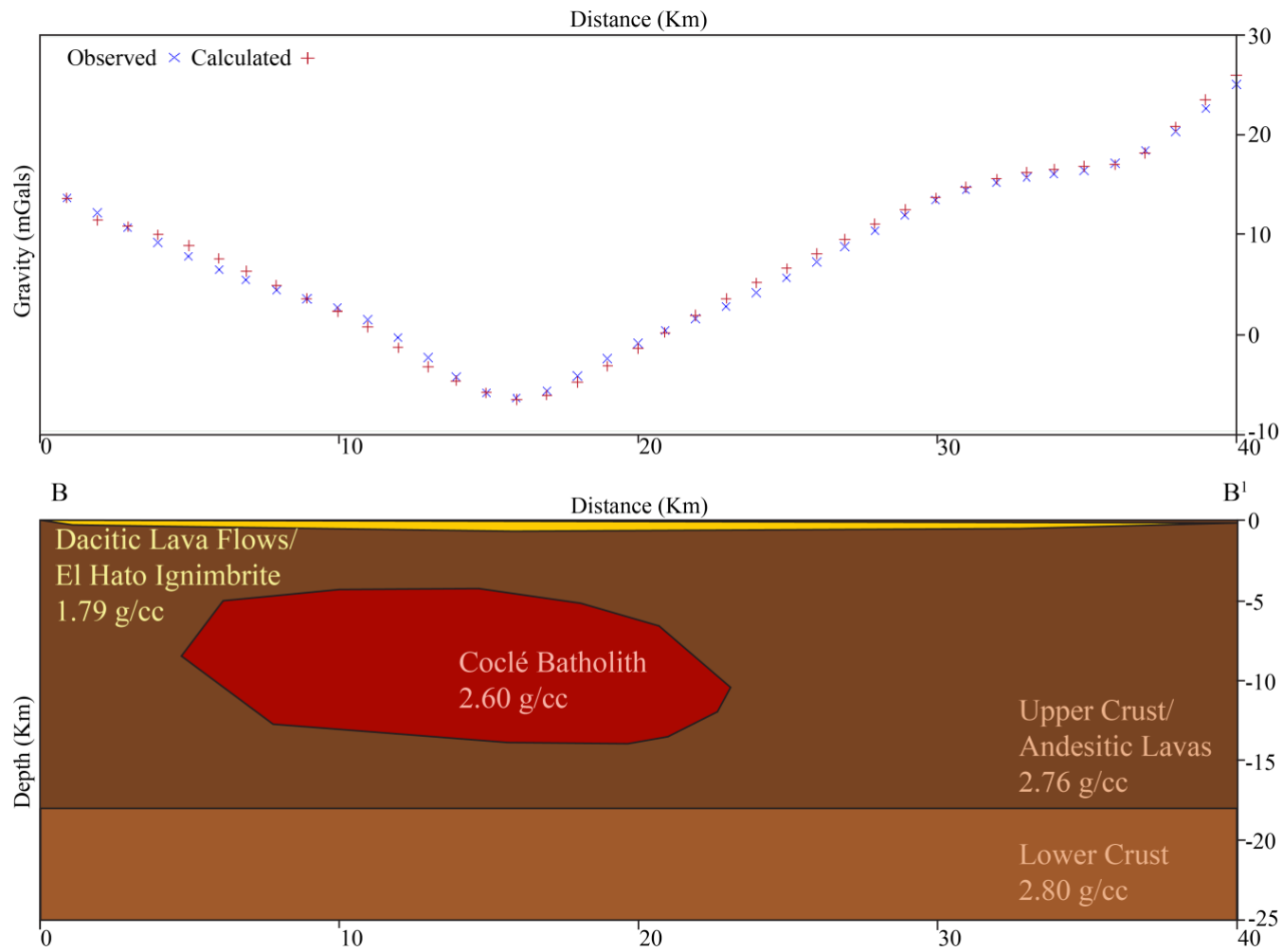
Figure 9: Gravity Model C, produced using Talwani. Transects C to C[1], running north to south across the volcano. Decreasing size of the Coclé Batholith correlates to the decreasing spatial extent of the low gravity anomaly seen in the western region of the volcano.

2.4 Results

The interpretation of gravity measurements was constrained by the production of 2.5 gravity models. The low gravity anomaly was first seen in a regional Bouguer anomaly map based on satellite data (Fig. 2). The high-resolution Bouguer anomaly map (Figure 4) shows the anomaly has additional structure. Transects were extrapolated from the data and used to produce 2.5-dimensional models across the volcano in an east to west, and a north to south orientation as illustrated in Figures 7-10. Gravity values were the most negative in the center of the volcano, specifically in regions of topographic depression. The values within El Valle and Sorá Calderas range between 0 to -11 mGals, these values increase with distance from the center of the volcano to values as high as 25 mGals.
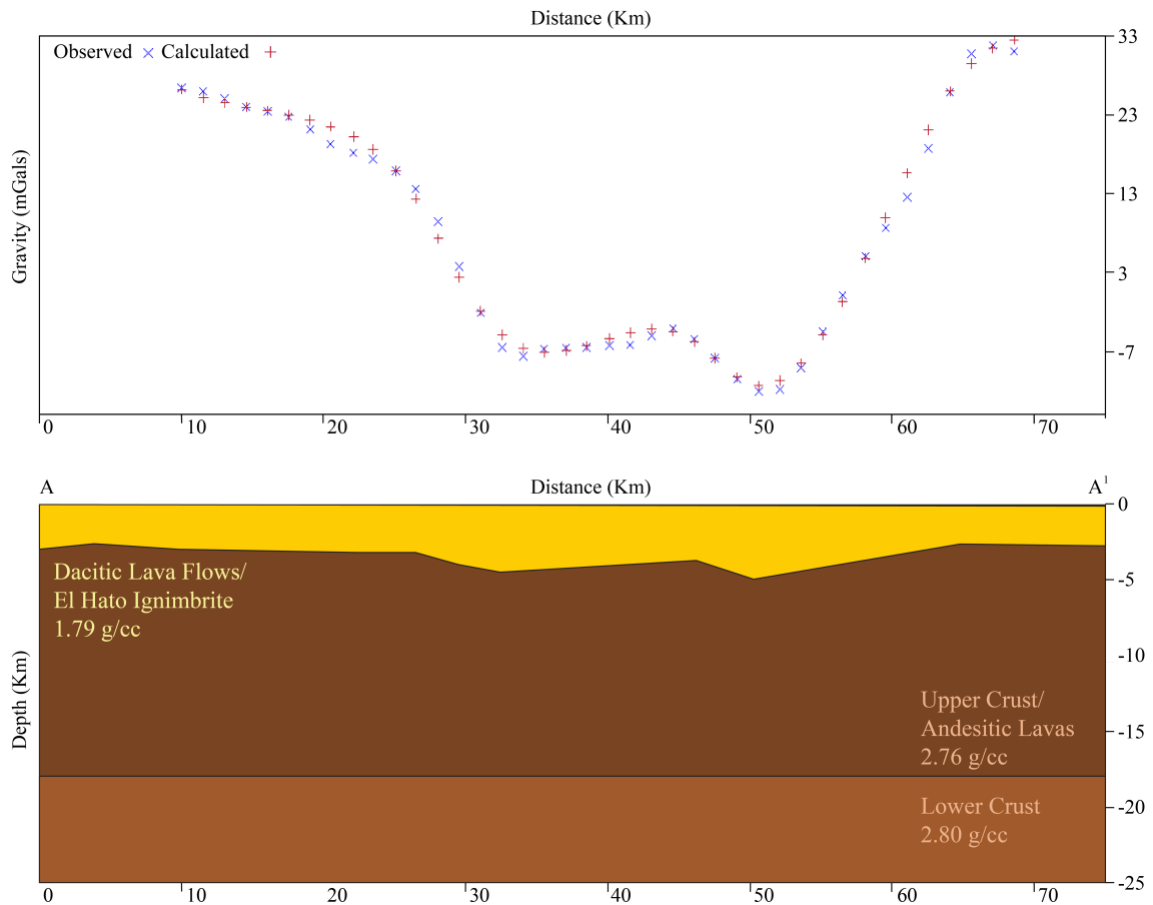
Figure 10: Gravity Model D, produced using Talwani. Transects A to A1, running west to east across the volcano and through the El Valle caldera. This model shows the necessary geometry required of the dacitic lava flows and El Hato Ignimbrite in order to produce the gravity signatures observed.

Table 1: Table of averaged density values for various samples from El Valle. Mapped geologic units are split into two different divisions for more simplistic gravity modeling.

Station #	Latitude	Longitude	Model Unit	Density in gr/cm^3	Std. Deviation
16EV010A	8.561	-79.950	Dacitic Lavas/Ignimbrites	2.35	0.01
16EV010B	8.561	-79.950	Upper Crust/Andesitic Lavas	2.65	0.01
16EV013	8.571	-79.985	Dacitic Lavas/Ignimbrites	2.04	0.08
16EV014	8.583	-79.993	Dacitic Lavas/Ignimbrites	2.45	0.01
16EV017	8.446	-79.989	Dacitic Lavas/Ignimbrites	1.56	0.07
16EV053	8.573	-80.173	Dacitic Lavas/Ignimbrites	1.30	0.01
16EV070A	8.560	-80.157	Upper Crust/Andesitic Lavas	2.67	0.00
16EV070B	8.560	-80.157	Dacitic Lavas/Ignimbrites	2.40	0.05
16EV071	8.565	-80.155	Dacitic Lavas/Ignimbrites	1.75	0.05
16EV083	8.545	-80.333	Dacitic Lavas/Ignimbrites	1.15	0.04
16EV084	8.557	-80.326	Upper Crust/Andesitic Lavas	2.98	0.04
16EV089	8.580	-80.275	Upper Crust/Andesitic Lavas	2.98	0.02
16EV097	8.586	-80.259	Dacitic Lavas/Ignimbrites	1.74	0.02
16EV099	8.554	-80.268	Upper Crust/Andesitic Lavas	2.64	0.13
16EV101	8.557	-80.249	Upper Crust/Andesitic Lavas	2.74	0.03
16EV103A	8.555	-80.224	Upper Crust/Andesitic Lavas	2.58	0.01
16EV103B	8.555	-80.224	Dacitic Lavas/Ignimbrites	1.27	0.04
16EV108B	8.569	-80.073	Upper Crust/Andesitic Lavas	2.65	0.01
16EV115	8.592	-80.106	Dacitic Lavas/Ignimbrites	2.43	0.07
16EV125	8.588	-80.157	Dacitic Lavas/Ignimbrites	2.28	0.12
16EV145	8.620	-80.102	Dacitic Lavas/Ignimbrites	1.12	0.07
16EV164	8.597	-80.029	Upper Crust/Andesitic Lavas	2.62	0.02
16EV166	8.607	-80.041	Upper Crust/Andesitic Lavas	2.77	0.02
16EV169	8.625	-80.050	Upper Crust/Andesitic Lavas	2.68	0.03
16EV171	8.645	-80.020	Upper Crust/Andesitic Lavas	3.06	0.45
16EV173	8.639	-79.997	Upper Crust/Andesitic Lavas	2.66	0.04
16EV278A	8.661	-79.939	Upper Crust/Andesitic Lavas	2.81	0.02
16EV286	8.708	-79.886	Upper Crust/Andesitic Lavas	2.87	0.03
16EV287	8.712	-79.880	Dacitic Lavas/Ignimbrites	1.59	0.05
16EV288	8.600	-79.889	Dacitic Lavas/Ignimbrites	1.46	0.18

The gravity models consist of 4 major units, the lower crust, uppers crust, batholith and the El Hato unit. The lowest unit in the model is the "Lower Crust" unit with a density of 2.80 g/cc which extends down to 25 kilometers' depth and overlies the mantle. The next unit is the "Upper Crust" with a density of 2.76 g/cc. This unit includes the upper crustal rocks of the Panamá Arc, as well as various andesitic lava flows associated with the old group pulse of

magmatic activity. The old group andesitic lava flows have similar densities to that of the upper crustal rocks, therefor they have been grouped together in a single unit for these models for computational simplicity. The batholith in the models, henceforth referred to as the Coclé Batholith, has been modeled with a density of 2.60 g/cc. The last unit in the model is the El Hato Unit/Dacitic pyroclastics with a lower density of 1.79 g/cc; surficial dacitic units have been grouped together with El Hato unit again to due to their similar densities.

The various models suggest that the large regional negative anomaly is unrealistically explained solely by low-density surficial units. Model D does fit the data, but it requires several kilometers of low-density volcanic rocks such as the El Hato in order to do so, whereas Hidalgo et al., 2011 indicates a maximum El Hato thickness of 110 m. In contrast, models A, B and C fit the observed gravity data using a large low density body beneath the volcano which is interpreted to be a silicic batholith with a density of 2.60 g/cc. These models better fit available surface data regarding the El Hato ignimbrite thickness. The low-density body is here termed the Coclé Batholith, and is interpreted to be about 35 kilometers east to west and about 20 kilometers in the north to south orientation. In terms of thickness, models A, B and C suggest the body to be located at between 3-14 kilometers' depth beneath El Valle (approximately 11 km thick in total). The presence of a large low density, and possibly warm batholith is plausible given that the volcano recently erupted at 0.35 Ma and produced large amounts of volcanic material that blanket the region at 1.33 Ma with the eruption of the El Hato Ignimbrite. The model suggests the low density El Hato unit is also likely a contributor to the anomaly and can be seen in Figures 7-9. The models also suggest that the El Hato ignimbrite extends about 30 kilometers east of the caldera and 30 kilometers west of El Valle de Anton. Gravity modeling suggest that the thickness of the El Hato reaches a maximum modeled thickness of about 800 meters thickest near the edifice of the volcano and thinning towards the Pacific coast. The gravity models can be affected by the modeled depth of the batholith and the thickness of the El Hato/Low Density material. When the batholith is modeled at shallower depths, the gravity signature gets lower, resulting in a thinner modeled thickness of the ignimbrite, and vice versa. The only previous estimate of the thickness of the El Hato unit was made by Hidalgo et. al (2011), suggesting the maximum thickness of the El Hato unit was 300 meters thick based on lithology exposures on the southern rim of the El Valle caldera.

In contrast to Figures 7, 8 and 9, Figure 10 shows the geometric parameters of the El Hato unit necessary to explain the Bouguer anomaly of the A to A^1 transect line. Without the low-density body beneath the caldera, the low density surficial unit would need to be much thicker to compensate for the gravity anomaly; with the modeled depth reaching a maximum of 4.5 kilometers thick and forming a caldera like structure across the volcano. Overall, Figure 10 suggests a configuration of the El Hato unit which is not geologically sound in comparison to previously published thickness estimates (Hidalgo et al., 2011). Therefore, the transects illustrated in Figures 7, 8 and 9 are more geologically plausible and are more likely to explain the low Bouguer gravity anomaly that characterizes the region.
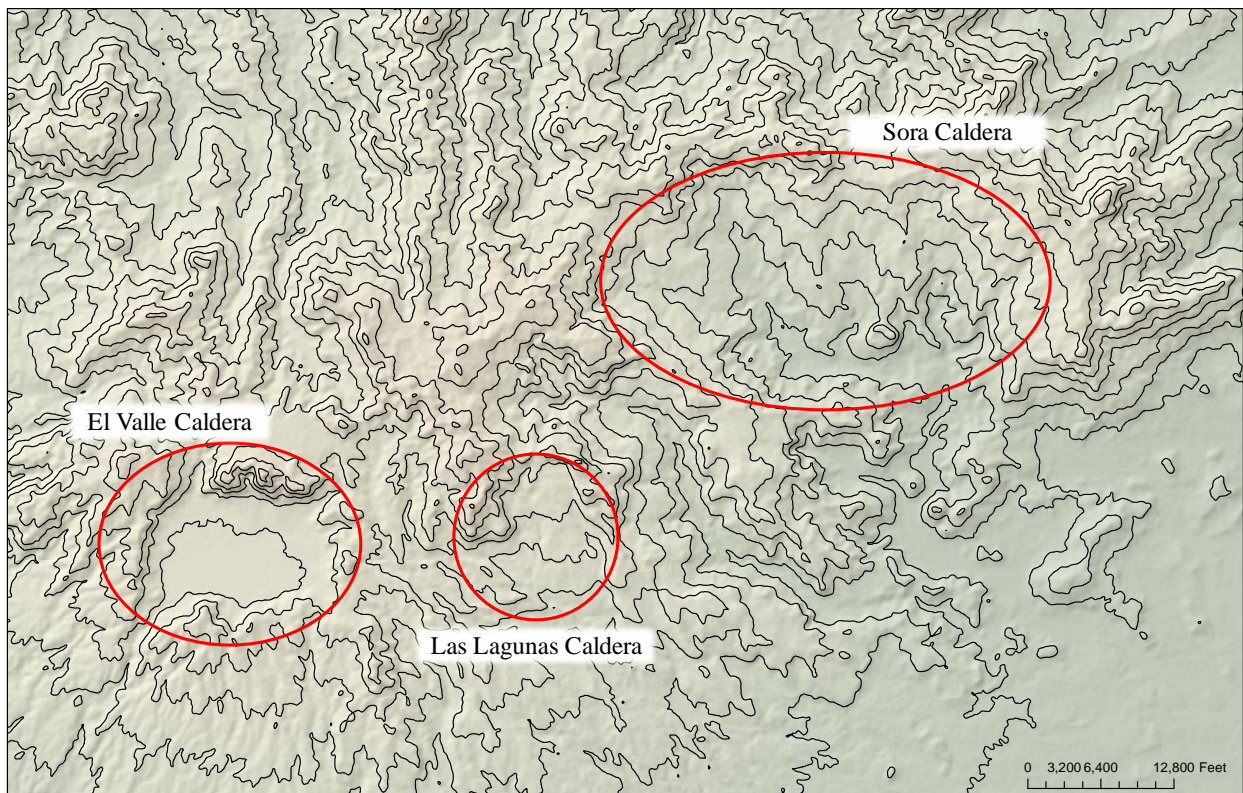
Figure 11: Topographic map of the eastern region of the El Valle volcano. Topographic depressions show areas on the volcano that exhibit caldera-like or bowl features which correlate to low gravity anomalies. From east to west, Sorá, the largest of the three depressions, Las Lagunas, the smallest, and the El Valle caldera which is most closely associated to the volcanic activity.

The gravity map (Figure 6) also indicates several regions of more negative gravity anomalies outside of the El Valle caldera that also correspond to topographic depressions. They are located around the towns of Las Lajas and Sorá. The topographic maps show ring like structures surrounding these depressions shown in Figure 11. The negative gravity anomaly suggests that within these structures there could be higher amounts of low density material. In

addition, the data suggest that there could be multiple caldera structures associated with Coclé batholith. However, the Sorá Caldera is filled with primarily andesitic rocks, and if the El Valle age/composition relationships hold for it, this indicates that the Sorá Caldera may be associated with the Old group volcanic rocks.

2.5 Discussion

The large negative Bouguer anomaly centered on the El Valle volcano can reasonably be explained by the influence of a large low-density sub-surface body in conjunction with the low density El Hato unit. Gravity models suggest that the Coclé Batholith is 35 kilometers wide, 5-10 kilometers thick and has been modeled with a "strike in-strike out" of 15 kilometers. The thickness of the El Hato unit reaches a maximum of 800 meters and thins with increasing distance away from the caldera. Evidence from gravity, as well as lithologic and topographic observations suggests that there are multiple calderas associated with the El Valle volcanic complex, with the other postulated calderas existing around the towns of Las Lagunas and Sorá (Figure 10). The caldera structures can be seen in gravity models of the 3 transects in Figures 6,7 and 8, suggested but the thickening of the El Hato formation in the two sections of the transect that correlate to the El Valle caldera and the Sorá caldera.
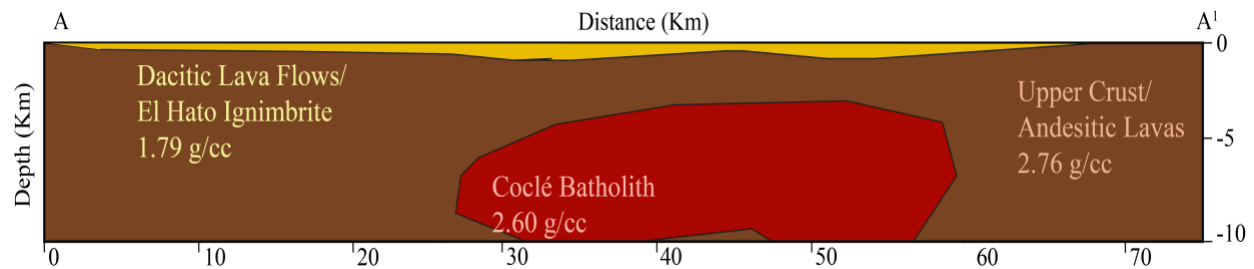
Figure 12: Close up cross section of the A to A[1] transect in Figure 7 to better illustrate the modeled caldera depressions of El Valle and Sorá (from west to east).

The modeled thickness of the Coclé batholith as constrained by gravity data correlates well with geothermobarometric measurements from Hidalgo et al, 2011. This provides an independent estimate for the thickness of the Coclé batholith. Using the Al-in-hornblende technique on magnesiohornblendes, Hidalgo et al., 2011, investigated the temperatures and pressures of amphibole crystallization associated with El Valle's most recent volcanic eruptions. Core and rim analyses on 33 hornblende phenocrysts from the Dacitic Domes, Iguana Pyroclastics and the El Hato unit were analyzed using the empirical thermobarometric

24

formulations by Ridolfi et al. (2010). Figure 13 displays the calculated temperature and pressure crystallization conditions of the young group volcanic rocks, which correlates to depths of 3.5 to 14 kilometers under pressures of 100 to 325 MPa. Overall, the depths derived from thermobarometric calculations correlate to the thickness of the Coclé Batholith suggested by gravity modeling. The correspondence of geophysical and geochemical observations (Figure 13) provides strong evidence of a large batholith beneath the El Valle volcano.
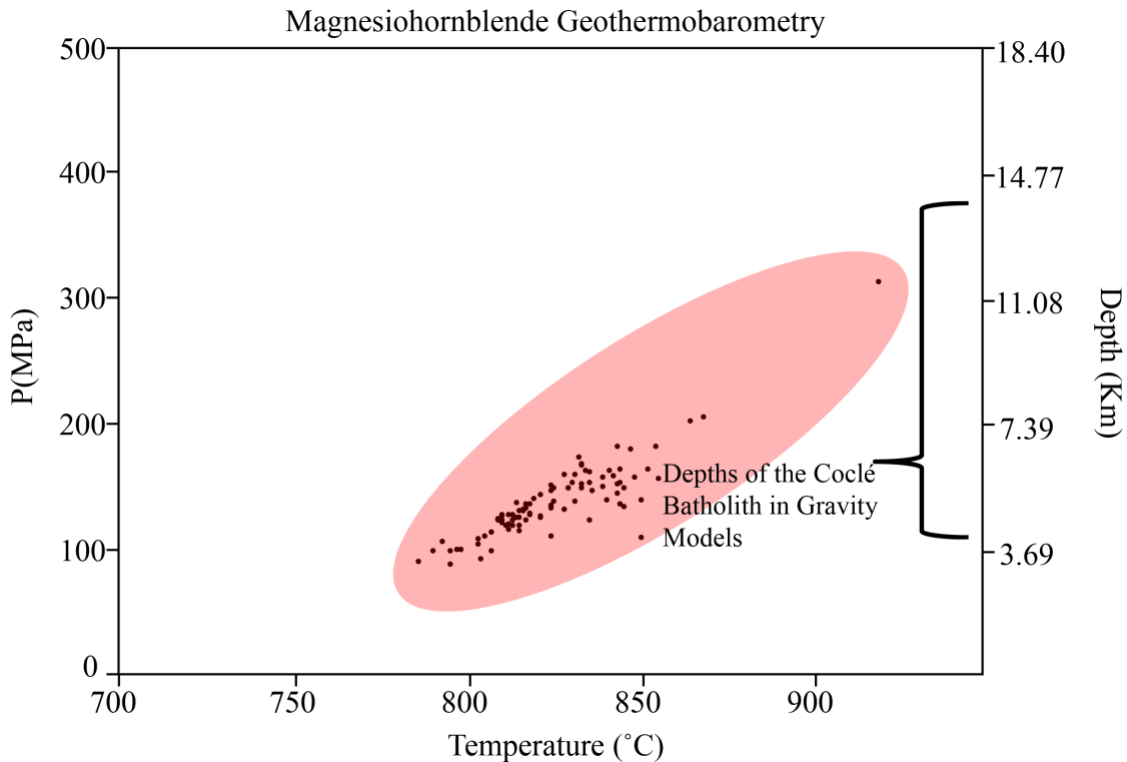
Figure 13: P-T-D configurations for El Valle amphiboles collected from young group lithologies, determined using amphibole geothermobarometry using calculation procedures from Ridolfi et al. (2010). Figure modified from Hidalgo et al. (2010).

Recent field investigations suggest the possibility of multiple caldera structures within the El Valle volcano. The main caldera, the aforementioned El Valle caldera, has previously been the only one associated with the El Valle volcano. On the eastern side of the volcano, there are apparent caldera wall like structures enclosing valley, bowl-like depressions; these features can be seen in the field and by using topographic maps (Figure 11). Just east of the El Valle caldera is the village of Las Lagunas, where a small lake is located in a bowl like depression surrounded by steep hills. Further east is the much larger depression, where the town of Sorá is located. These topographic structures could either be an artifact of previous eruptive events, or

could indicate a slight westward migration of volcanic activity over the history of the Coclé batholith.

2.6 Conclusion

Detailed gravity investigations of the El Valle volcano identify the existence of a large negative Bouguer gravity anomaly. Modeling of the anomaly indicates that low-density surficial units alone cannot realistically explain the magnitude of the gravity low. Instead, a combined signature from both surficial lithologies and subsurface features is needed. Gravity data was collected in the summer of to 2016 to produce multiple transects across El Valle de Anton and radially around the volcano. Data was corrected and extrapolated to generate a high resolution Bouguer anomaly map, which was then used to produce multiple 2.5-dimensional gravity models. Lithologic and geophysical investigations on the El Valle volcano provide insight on the surficial and subsurface geometry. Field lithological investigations coupled with low gravity Bouguer anomalies imply there could be multiple caldera structures associated with the El Valle volcano. In addition to the main caldera, where the town of El Valle de Anton resides, there are at least two other areas of interest. The regions where Las Lagunas and Sorá are located show caldera-like depressions in topography associated with circular low gravity anomalies likely influenced by the low-density material, such as dacitic lava flows or ignimbrite. 2.5-dimensional gravity modeling performed in the Talwani program suggest that the primary cause of the gravity anomaly is due to the presence of a large low density silicic body located beneath the volcano, and partly due to low density young group volcanics blanketing the region and filling in the aforementioned caldera features with thickness ranging from 0 to 2 kilometers. The Coclé Batholith is about 35 kilometers E-W and 20-30 kilometers wide N-S and 10 kilometers thick as implied by the gravity models. The modeled depths of the Coclé Batholith is similar to calculated hornblende crystallization pressures providing cohesive petrological and geophysical evidence for a large batholith beneath the El Valle Volcano and associate region. In conclusion, lithologic, geophysical, and petrological data supports the placement and geometry of the Coclé Batholith underneath the El Valle volcano in central Panamá.

CHAPTER 3

GEOCHEMICAL INSIGHTS INTO THE PETROGENIC EVOLUTION OF THE EL VALLE VOLCANO, PANAMÁ

3.1 Abstract

The Panamá Arc is one of the most tectonically unique locations on the planet. Of the three volcanoes located in Panamá, El Valle is the eastern most extent of the modern Central American Volcanic Arc. El Valle is characterized by two distinct periods of magmatism; with a Young Group (3-0.03 Ma) and an Old Group (5-15 Ma) composed predominantly of dacites and andesites, respectively. The younger volcanic units are silica rich, moderate MgO content, with high Sr/Y and La/Yb ratios and exhibit an overall adakitic composition. Previous investigations show a decrease in HREE concentrations with decreasing age. The petrogenetic conditions which led to the different geochemical signatures between the Young and Old volcanic groups has been a topic of debate. Overall, the cause for the change is not well constrained. However, hypotheses vary from relating to subduction erosion of the Cocos plate beneath Central America (Goss and Kay, 2006), to slab-window processes (Abratis et al., 2001), or to CLIP basement involvement. Geophysical evidence suggest that a modern Benioff Zone does not exist beneath the southern boundary of the Panamá Block (e.g. Trenkamp et al. 2002). Alternatively, Rooney et al. (2015) has proposed the occurrence of oblique subduction as being responsible for the adakitic (Young Group) geochemical characteristic. However, fractional crystallization modeling of new ICP-MS geochemical data suggests that the adakitic geochemical signature of the Young volcanic group can be the result of partial melting of basal arc crustal material, followed by the fractional crystallization of the melted material. The proposed model offers a possible explanation for the unique chemical transitions observed in Panamá and the transition between Young and Old group geochemical signatures may have been triggered by slab-detachment.

3.2 Geologic Setting and Magmatic History

The region that encompasses Panamá is one of the most complex tectonic environments in the world, due to the interactions between the Panamá block, and the Caribbean, South American, Cocos and Nazca plates. The Panamá Arc initially formed as an intra-oceanic island arc system on the trailing edge of the Caribbean Plate (Buchs et. al. 2010) at

approximately 73 Ma, due to initiation of Farallon Plate's subduction beneath the Caribbean Large Igneous Province (Gerya et al., 2015). The age of arc initiation is placed at 73 Ma as Buchs et al. (2010) has documented basaltic dikes in the Azuero Peninsula exhibiting subduction related signatures at that time. The initial Panamá arc existed though the Eocene, followed by a quiescence of magmatic activity during the Oligocene (Wegner et al., 2011; Farris et al., 2011; Montes et al. 2012). Magmatic activity resumed from the late Oligocene to the Miocene with the emplacement of lavas, dikes and intrusives which are considered part of the Cordilleran Arc of Wegner et al. (2011). These rocks range from basalt to rhyolite and from gabbro to granite (Wegner et al., 2011). During the Miocene, collision began between the Panamá arc and the South American Plate at approximately 23-25 Ma (Farris et al., 2011). Around this time, the Farallon plate split into the Cocos and the Nazca plates (Lonsdale, 2005). A geochemical change can be observed in the Panamá arc at 23-25 Ma; which occurs concurrently with the exhumation of Panamá and the Columbian Andes, implying arc collision occurring at this time (Mora, 2010; Farris et al., 2011).

These events resulted in the amagmatic nature in parts of eastern Panamá with the exception of the Maje Range and Pearl Islands and left western Panamá characterized by adakite-like, nonstandard arc magmatism (Farris et al., 2011). The exact age of collision has been a topic of debate, with proposed ages ranging from 38- 40 Ma (Barat et al., 2014) to 12 Ma (Coates et al., 2004). The arc formed due to subduction of various Pacific Plates (first the Farallon, and then the Cocos and Nazca), however at some point northward subduction ceased. Probably the best record of when this happened comes from linear magnetic anomalies surrounding the Sandra rift south of Panamá. Lonsdale (2006) examined linear magnetic data and suggests that northward spreading on the Sandra rift ended at approximately 8 Ma. This also corresponds with formation of the Panamá Fracture zone.

One contrary piece of evidence regarding the termination of northward subduction, is the fact that modern and near modern volcanism at El Baru and El Valle contain subduction zone signatures, such as negative, Nb-Ta anomalies, depletion of high field strength elements and enrichment of large ionic lithophile elements and, despite geophysical data, some researchers suggest that subduction is still occurring on the southern Panamánian margin (e.g. Defant et al., 1992, Hidalgo et al., 2012; Rooney et al., 2015). Rooney et al. (2015) suggest that oblique subduction has been occurring since the termination of the Sandra Rift 8 Ma. The most recent

volcanism in Panamá contains adakite-like signatures, with elevated Sr/Y ratios steep REE patterns with strongly depleted HREE and moderate MgO content. Initial workers interpreted this signature to have resulted from slab melting (Defant et al.,1992). This signature is present is volcanic rocks younger than 3-4 Ma, and some characteristics occur in rocks as old as 8-10 Ma, suggesting that it may be related to the cessation of northward subduction.

Initial arc volcanic rocks are hydrous, relatively depleted in REE, but have a larger Nb-Ta anomaly indicating strong fluid flux from the slab into the mantle wedge. The depleted magmatism persisted until about 25 Ma within the Panamá Canal Zone. These older arc rocks range from calc-alkaline to tholeiitic, with basaltic to andesitic compositions. In addition, the rocks are dominantly hornblende bearing (Rooney et al. 2010), with LILE enrichment and moderate HREE concentrations, indicative of hydrous mantle wedge derived magmas (Pearce and Peate, 1995).

Between 30 to 40 Ma, there was a hiatus of magmatic activity with resumption of arc volcanism by 25-30 Ma. These rocks are predominantly granodioritic plutonic rocks and andesitic-dacitic volcanic rocks. Among these, the largest intrusive bodies are the Petaquilla batholith, located about 78 kilometers northwest of El Valle, and Cerro Colorado located about 100 kilometers west of Petaquilla. The Petaquilla batholith hosts porphyry copper-gold deposits and was the first place in Panamá copper mineralization was discovered, sparking geo-economical interest region (Whattam et al. 2012).

Western Panamá rocks younger than 10 Ma, exhibit a low HREE signature with higher La/Yb ratios. The younger Miocene arc magmatism is characterized by lower REE values and higher concentrations of LILEs (Wegner et al. 2011). The youngest episode of volcanism in Panamá, occurring after 3-4 Ma, contains an adakitic signature with elevated Sr/Y ratios steep REE patterns with strongly depleted HREE and moderate MgO content. The reason for the transition in geochemical signatures is not completely known, however multiple theories exist (e.g. the existence of a slab window, oblique subduction, slab-melting or subduction erosion of Galapagos material). One significant quandary is that geochemical evidence suggests the existence of subduction, whereas geophysical data indicate a lack of a pronounced Benioff Zone. Overall, geochemical modeling presented below suggests that the Young group geochemical signatures can be reproduced via the partial melting of Cretaceous-Early Tertiary lower crustal arc rocks.

Geologic History of El Valle

The El Valle volcano, located in Central Panamá, is the easternmost volcano in the Central American Arc (Figure 1). The base of the volcano is blanketed with Quaternary ignimbrite deposits extending southward from the volcano towards the Pacific coastline (the El Hato ignimbrite). At the summit, is a 20 km^2 caldera where the town of El Valle de Anton is located. The oldest eruptive unit exposed within the caldera is the Gaucamayo Dacitic Flow, which has an K-Ar age of 10.19 ± 0.37 Ma (Defant et al., 1991). Other early (Old group) eruptive units include the Piedra Fine Grained Andesite, the Piedra Coarse Grained Andesite (K-Ar age of 6.92 ± 0.53 Ma), the Llano Tigre Andesite (Ar-Ar age of 5.14 ± 0.34 Ma) and the Rio Anton and Iguana pyroclastic flows (Defant 1991a, Hidalgo et al, 2011). A 3.5 Ma period of quiescence followed the eruption of the Llano Tigre Andesite, which ended at 1.55 Ma with the emplacement of a dacitic dome that overlooks the El Valle Caldera. Shortly after, at approximately 1.33 Ma, the eruption of the extensive El Hato Ignimbrite occurred, covering the flanks of the volcano south of the edifice. This eruption likely led to formation of the modern El Valle Caldera followed by the continued eruption of the east-west orientated dacitic domes from 1.55 Ma (Defant et al., 1991a). Such younger group units are dominantly dacitic, hornblende bearing, have low HREE values, and high Sr/Y ratios. Following the collapse of the El Valle caldera, El Hato ignimbrite derived sediment was reworked and deposited as the El Valle formation. Defant et al., 1990, interprets the El Valle formation as a lacustrine deposit that reaches more than 800 meters of thickness inside the caldera, suggested from gravity models presented in Chapter 2.

Recent field lithologic investigations suggest the possibility of multiple caldera structures with in the El Valle volcano. The main caldera, the aforementioned El Valle caldera, has previously been the only one associated with the El Valle volcano. However, on the eastern side of the volcanic edifice, wall like structures enclose and form bowl-like depressions, and are potentially additional caldera structures. These features can be seen in the field and by using topographic maps (Figure 11). There are also 5-10 mGal negative gravity anomalies associated with the topographic features. Just east of the El Valle caldera is the village of Las Lagunas, where a small lake is located in a bowl like depression surrounded by steep hills. Further east is a much larger depression, where the town of Sorá is located. These structures could either be an

artifact of previous eruptive patterns, or could indicate a westward migration of volcanic activity during El Valle's geologic evolution.

3.3 Methods
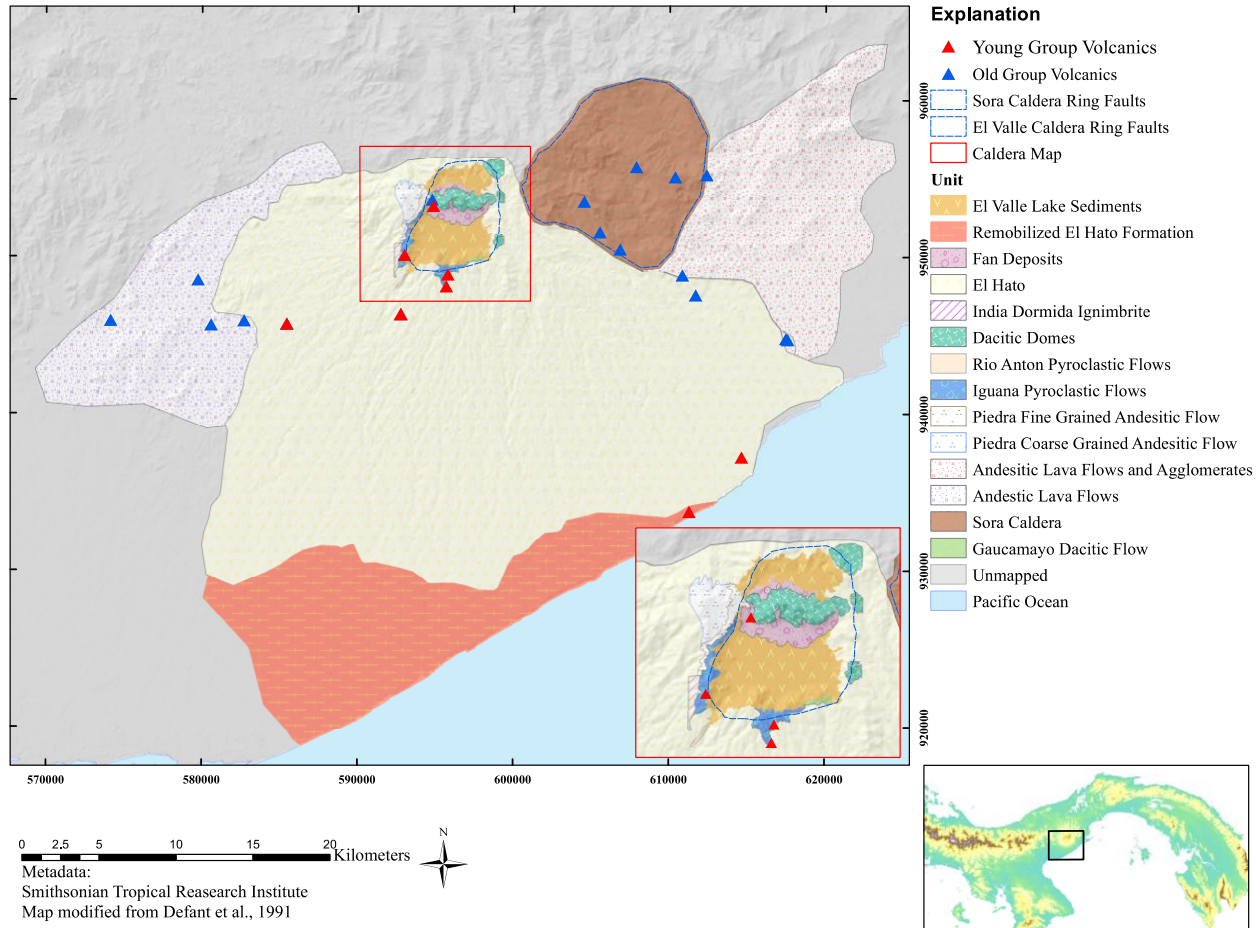
Figure 14: Locations for geochemical samples used in the study are showed on the map using red and blue triangles representing young and old group volcanics, respectively.

3.3.1 Lithologic Sampling

In July of 2016, lithologic observations and samples were collected from the various rock units associated with the El Valle volcano. With the new geologic data, an updated geologic map was constructed, modified from Defant et al. 1990 (Figure 1). Sample locations are plotted in Figure 14, and samples were collected to perform geochemical analyses and lithologic descriptions. Samples were taken from as many of the proposed geologic units as possible to provide the best data coverage. Due to the humid tropical environment, weathering of the rock units was prevalent, and sampling had to be done carefully to obtain fresh material.

3.3.2 Trace Element Geochemical Analysis

Trace element analyses were conducted at the National High Field Magnetic Laboratory using the Element2 ICP-MS. Whole rock samples were powered using an aluminum oxide shatter box to produce 20 to 30 mg of rock powder and was then properly weighed and distributed into Teflon beakers. Rock powders were dissolved inn closed Teflon beakers using 3-4 ml of (3:1) distilled $HF:HNO_3$ for ~48 hours (or until fully dissolved) at 100°C; once dissolved, acid was evaporated at 100°C. The samples are then redissolved in ~1ml of concentrated HNO_3 for ~48 hours (or until fully dissolved) at 100°C, and then dried at 100°C. The samples are then redissolved using 2 ml of 7N HNO_3 and submerged in an ultrasonic bath for 30-60 minutes; once dissolved samples are dried at 100°C. Samples are then dissolved in a measured volume of 7N HNO_3 and quartz-distilled H_2O is added so the resulting solution is 2% nitric with 500ppm of total dissolved solids. This solution is then diluted to a working solution of 200ppm total dissolved solids using 2% HNO_3. Indium is added to the solution as an internal standard at a concentration of 1 ppb. These solutions where then analyzed on the Thermofisher Element 2 inductively coupled mass spectrometer in relation to USGS rock standards (BHVO-1, AGV-1, DNC-1, W2). Trace element concentrations are reported in Table 4 of Appendix C

3.3.3 Major Element Geochemical Analysis

Major element geochemical analysis was conducted using X-Ray Fluorescence Spectrometry (XRF) via ALS-Chemex. The samples were powdered, mixed with a lithium borate flux, and then fused into glass discs. The samples were then analyzed using XRF to measure major element weight percent using NCSDC73303 and OREAS 13b as standards. In addition, a samples mass was measured before and after initial heating to measure loss-on-ignition (LOI). Major element compositions are reported in Table 3 of Appendix B.

3.4 Geochemical Results

3.4.1 Major Element Geochemical Data

The Young Group volcanic rocks are more silica rich (SiO_2), between 65-70% (weight percent), less than 2% MgO, between 15.5 to 17.5% Al_2O_3. Old Group volcanic rocks silica content has a wider range, with weight percentages between 53-70%. MgO wt. % range between .5-4.5% and Fe_2O_3 wt. percentages between 4-10.5%. While there is a range in major element

oxides observed in the Old Group volcanics, the plotted samples exhibit two grouping patterns within the sample set. Differences between the Old and Young Group volcanics' chemistries can also be seen in Figures 15, 16 and 17. Generally, the Young Group has less geochemical variation and plot near other young group volcanic rocks studies by Defant, et al. (1991), Hidalgo, et al. (2011), and Farris, et al. (2011). The Old Group exhibits a greater geochemical range, which reflects the larger mineralogical differences in the samples from Panamá. Lithologic observations tell that there are differences in the mineralogies present in the Old Group andesite. The andesite contains clinopyoxene, orthopyronxe, plagioclase, and iron titanomagnetite. However, some of the rocks, in formations Miocene Andesitic Lavas (Mal) contain biotite, while the andesites in Miocene Sorá Caldera (Msc) and Miocene Andesites and Agglomerates (Maa) do not contain biotite. In addition to mineralogical differences, biotite containing andesites also exhibit higher SiO_2 and lower CaO, MgO, MnO and K_2O compositions by weight percent. Finally, both Young and Old group volcanics exhibit low TiO_2, which is common to subduction zone magmas (Defant et al., 1991).

3.4.2 Trace Element Geochemical Data

The trace element signatures observed in the samples from El Valle are typical of volcanic arc signatures apart from a few characteristics unique to adakite like magmas. The samples exhibit varying depletion of high field strength elements (HFSEs) and enrichment of large ionic lithophile elements (LILEs) and Nb/Ta anomaly, all typical of subduction zone magmas (Figure 18). A majority of these samples also exhibit Sr enrichments, typical of volcanics within the Central America Volcanic Arc (Rooney et. al, 2015) (CAVA; citation). Young Group magmas show an increased depletion in heavy rare earth elements, as well as an increase in Sr/Y and La/Yb ratios (Figure 19). These geochemical characteristics are unlike ignimbrite units elsewhere in the CAVA (Hidalgo et. al. 2011). Trace element chemistry data normalized to Bulk Silicate Earth (McDonough and Sun, 1995) in Figure 18 illustrates the contrasting characteristics of the Young and Old Groups.
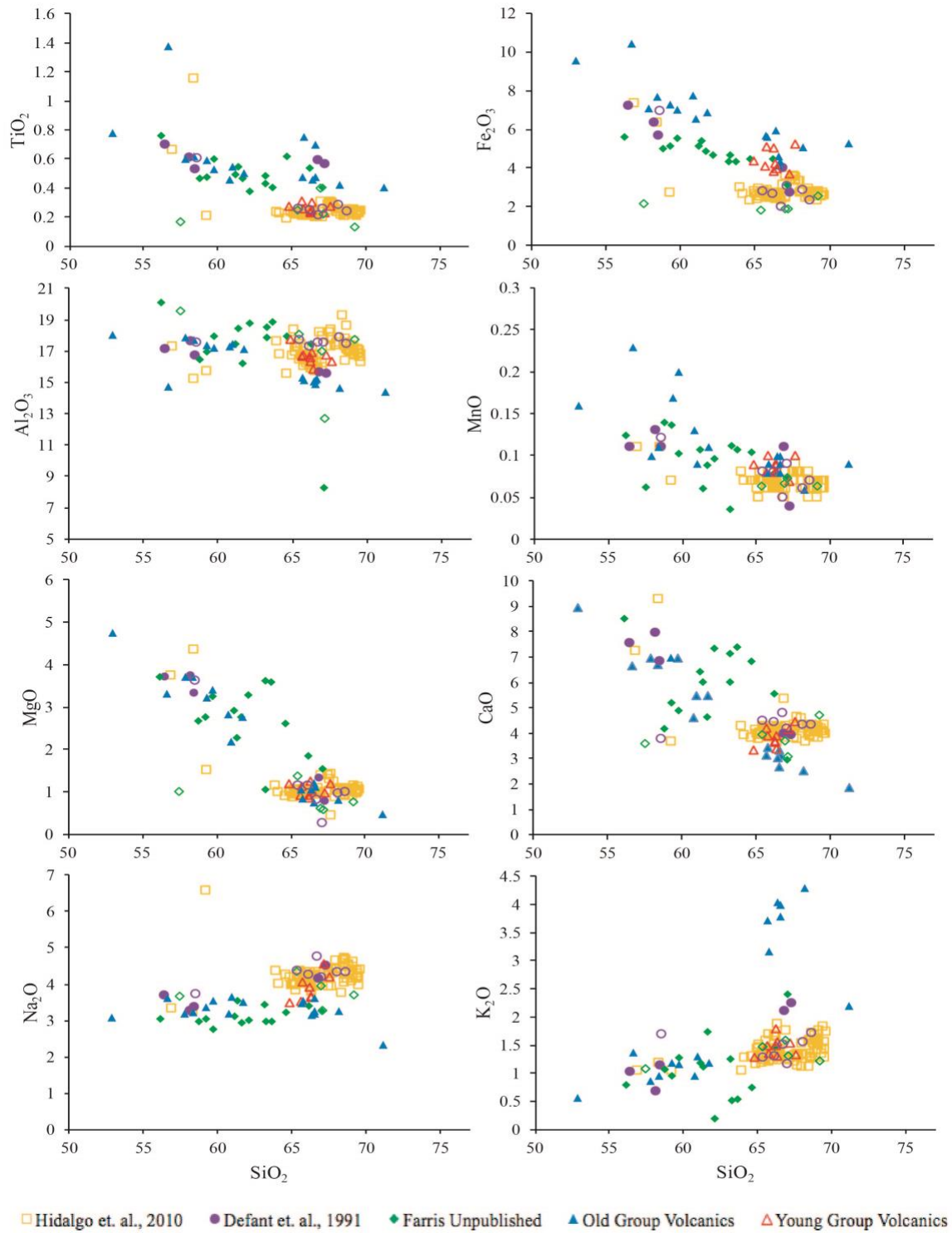
Figure 15: Harker Diagrams for El Valle samples from the current study, Farris unpublished, Hidalgo et al., 2011 and Defant et al., 1991.

3.5 Discussion

3.5.1 Major Element Geochemical Modeling

On the Ewart et al., 1982 and LeBas et al., 1986 classification diagrams samples from the El Valle region range from basaltic andesite to dacite within the low-K and calc-alkaline magma series (Figure 16 and Figure 17 respectively). The Old Group volcanics predominantly plot in the andesite and the calc-alkaline fields. The Young group volcanics plot in the dacite fields, and fall in the calc-alkaline field.
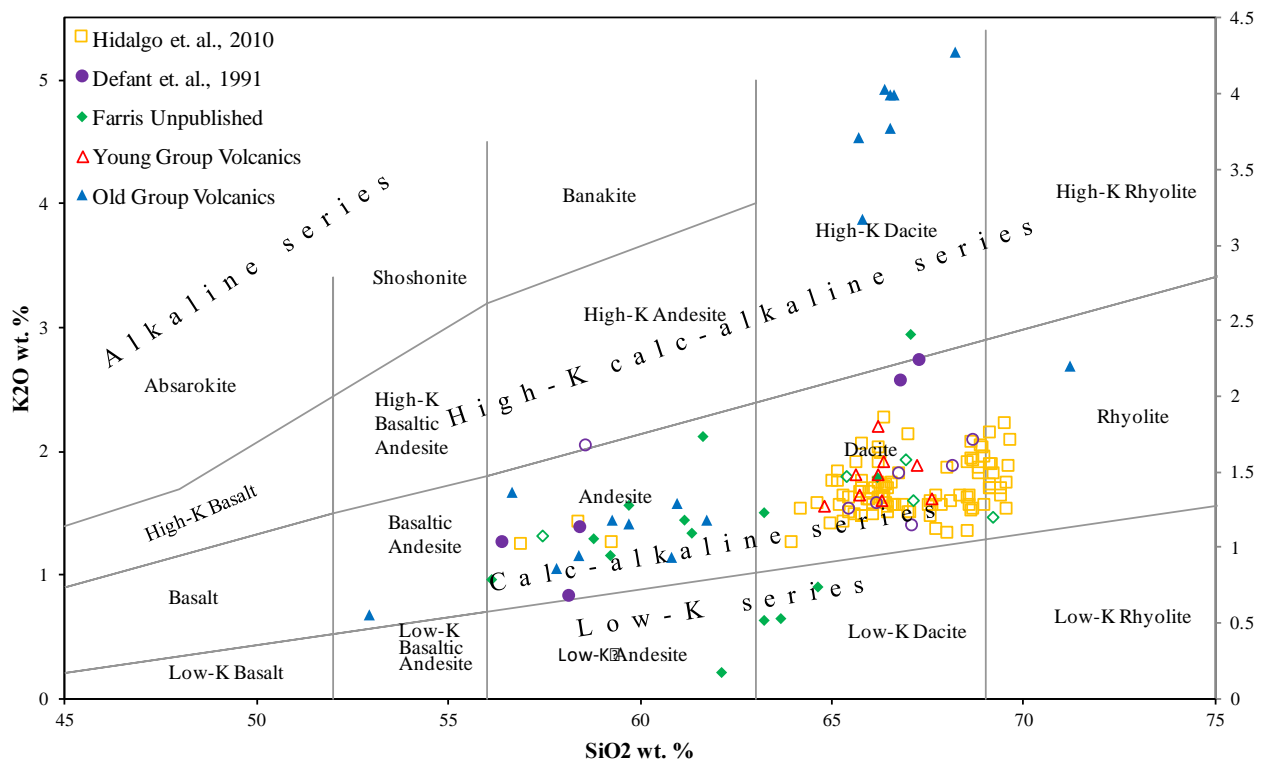
Figure 16: K_2O vs. SiO_2 discrimination diagram from Ewart et al. (1982) Diagram shows that most of the Young Group samples (Red Triangles) plot in the dacite fields, while Old Group samples (Blue Triangles) show samples predominately in the andesite and high-K dacite. All samples are calc-alkaline.

Differences between to the Old and Young Group volcanics' chemistries can also be seen in Figure 15. Generally, the Young Group has less of a geochemical variation and plot near other young group volcanics studies by Defant, et al. (1991), Hidalgo, et al. (2010), and Farris, et al. (2011). The Old Group exhibits a larger range in geochemical signatures and mineralogies.. Lithologic observations tell that there are differences in the assemblage of crystallizing phases in the Old Group andesites. The andesites contain clinopyroxene, orthopyroxe, plagioclase, and

35

iron titanomagnetite; however, some of the rocks, in formations the Miocene Andesitic Lavas (Mal) contain biotite, while the andesites in Msc do not contain biotite. In addition to mineralogical differences, biotite containing andesites also exhibit higher SiO_2 and lower CaO, MgO, MnO and K_2O compositions by weight percent; both Young and Old group volcanics exhibit low TiO_2, common of subduction zone magmas.

Figure 17: Total alkali vs. silica content of El Valle samples from various studies, after Lebas et al., 1986.

Figure 18: Spider element diagram for the El Valle samples; Young Group in red and Old Group in blue.
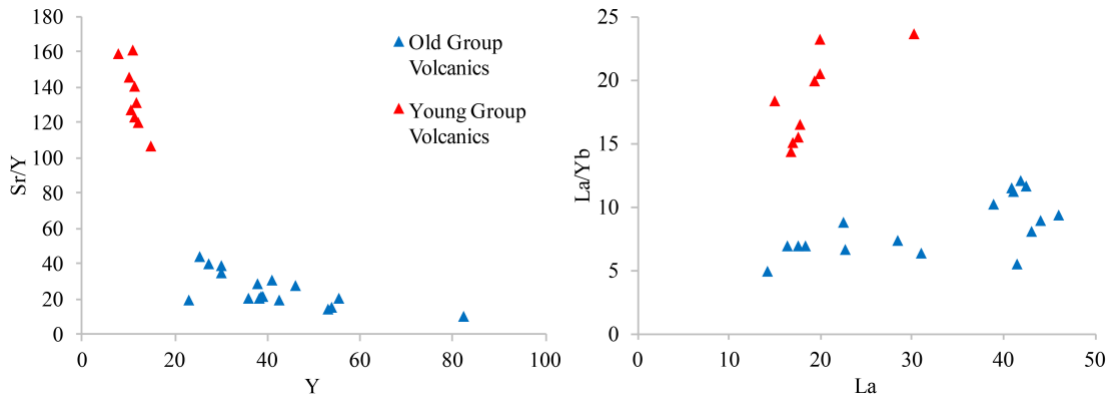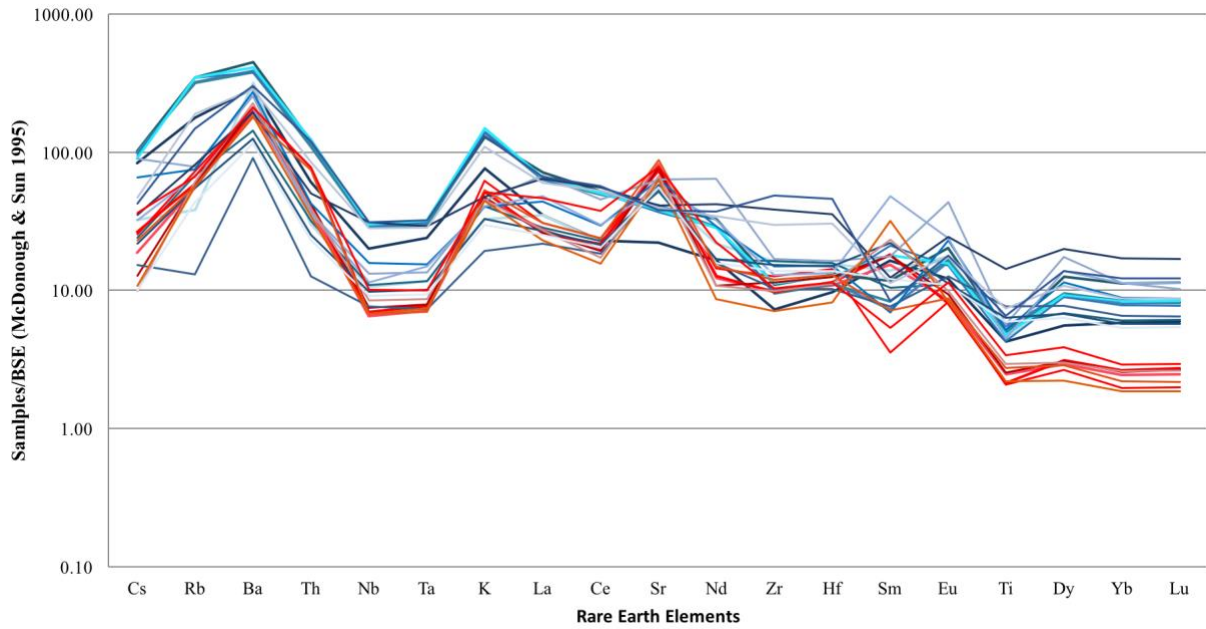
Figure 19: La/Yb vs Yb and Sr/Y vs Y plots show the transition into adakite like characteristics, illustrated by the increasing ratios.

3.5 Geochemical Modeling

3.5.1 Major and Trace Element Geochemical Modeling

To better understand the transition between the Old and Young Group geochemical signatures, trace element modeling was utilized. Fractional crystallization models were used to help determine the original source material of the Young Group Volcanic rocks. The two contrasting hypotheses to be tested are the melting of a subducting slab and the melting of arc crust. Both scenarios were modeled to determine which would yield trace element distributions

37

analogous to the Young Group volcanic rocks seen in Figure 18. Major element chemistry was also used to determine theoretical mineralogical compositions using MELTS to be utilized in fractional crystallization models to help postulate the petrogenetic history of the Young Group Volcanics. In order to model these geochemical parameters, two-stage calculations were carried out in order to obtain the hypothetical geochemical signatures. The first step is to establish what the initial composition was (i.e. what is the initial material undergoing fractional melting), in these models the initial compositions used were a basaltic eclogite average (Zhang et al., 2008) altered Mid Ocean Ridge Basalt (MORB) from subduction (Stracke et al., 2016) and arc intrusives from the Kuna Yala, Panamá (Farris, unpublished); representative of subducted crust and lower Panamá lower crustal values, respectively. Once an initial composition has been selected, a fractional melting equation (equation f.) can be used to determine what the trace element abundances would be if an initial composition, undergoes a certain amount of fractional melting.

    f.

$$\frac{C_L}{C_0} = \frac{1}{F}[1 - (1 - F)^{1/D_0}$$

    g.

$$\frac{C_L}{C_0} = F^{D_0 - 1}$$

Using the incremental values calculated from the fractional melting equation (F=10% melting, 20% melting, ect.), the concentrations of the melt are then used as input to the fractional crystallization calculation (equation g.). The product of this equation calculates the theoretical trace element concentrations of a rock, after the source has experimentally undergone various amounts of fractional melting and crystallization.
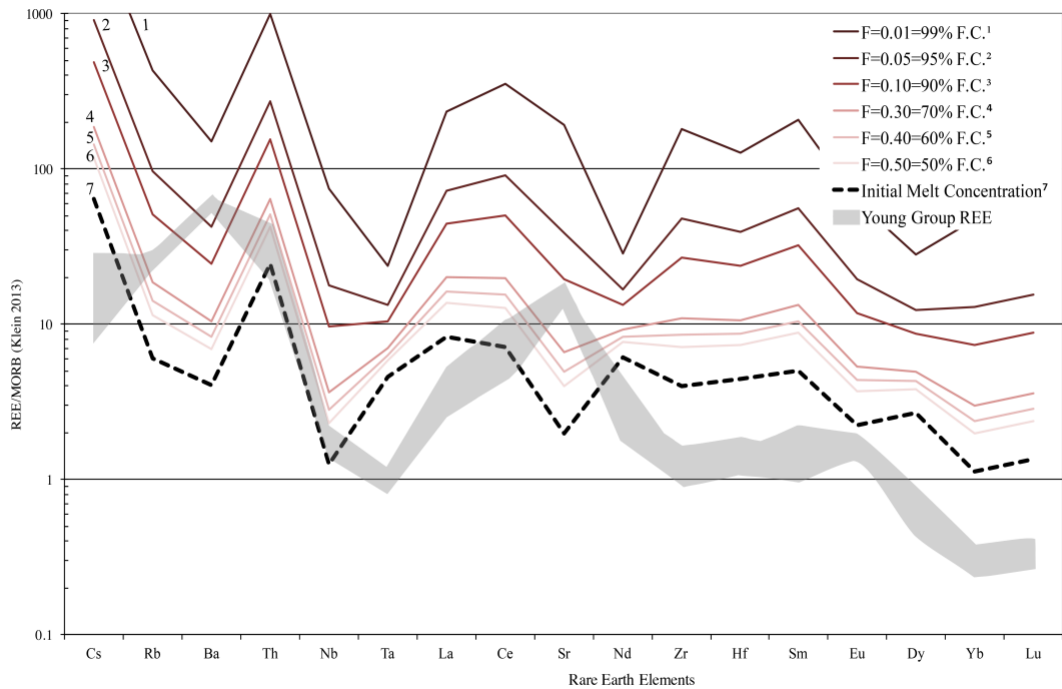
Figure 20: Fractional crystallization model showing trace element signatures after basaltic eclogite has undergone 60% fractional melting before crystallization. This model is not deemed successful.
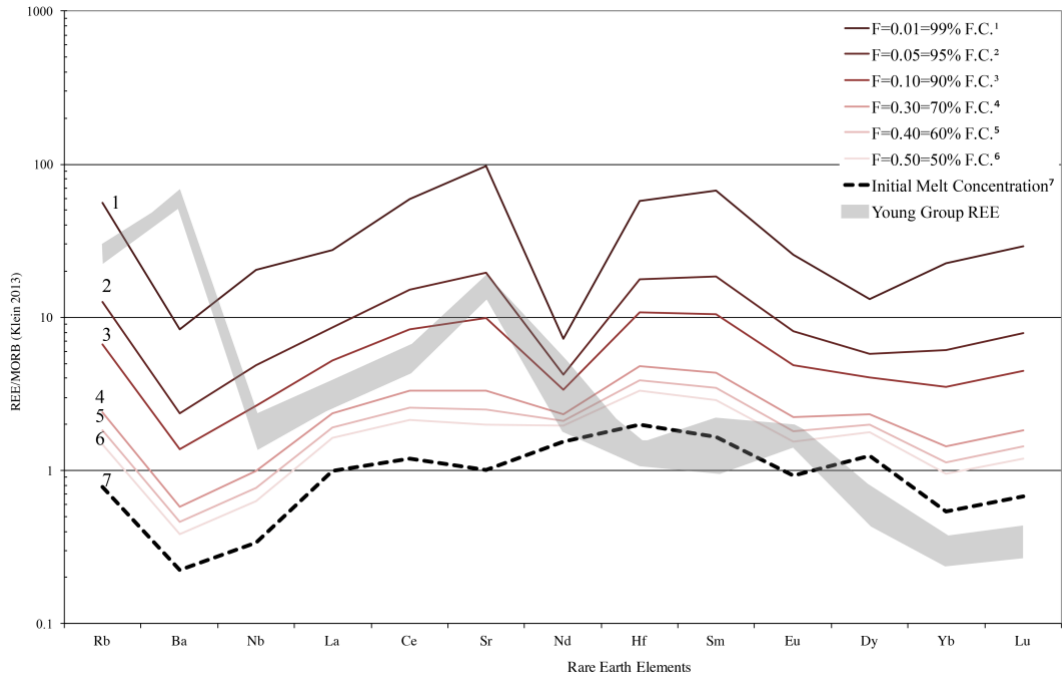
Figure 21: Fractional crystallization model showing trace element signatures after MORB modified by subduction has undergone 50% fractional melting before crystallization. This model is not deemed successful.

Modal mineralogies of the initial and end compositions are needed in the models in conjunction with the appropriate partition coefficients. The calculated concentrations were then compared to the trace element concentrations of El Valle Young Group samples to see if modeled conditions could provide a hypothesis, as to what geologic events could have produced the unique geochemical observations at El Valle.
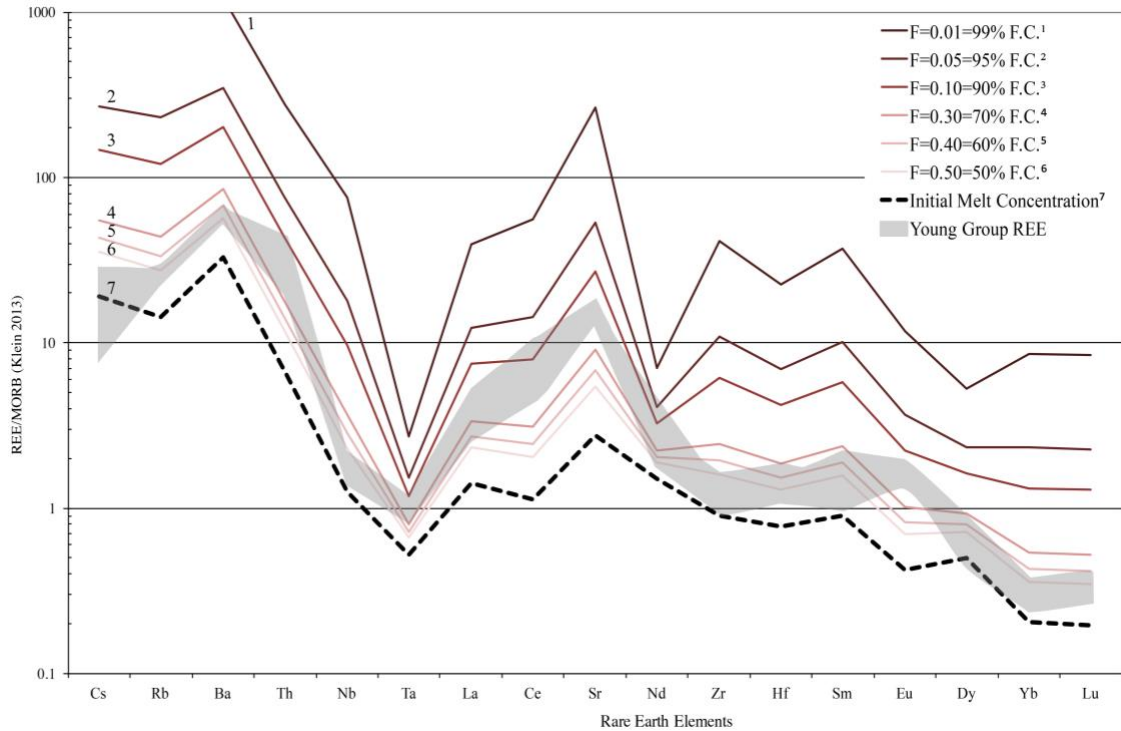
Figure 22: Fractional crystallization model showing trace element signatures after lower crustal material has undergone 30% fractional melting before crystallization. This model produced reasonable signatures and could explain what it observed in Panamá.

MELTS was used to calculate theoretical modal mineralogies for the initial compositions in both scenarios. When using the average basaltic eclogite and altered MORB as a starting material, trace element signatures could not be reproduced. This could mean that the Young group's signature was not due to melting of subducted crust, or it could be an artifact of the data used in the models (Figure 20 & Figure 21). However, reasonable results did come from using lower crust as a starting composition (Figure 22). Per the produced models, lower arc crust with a modal mineralogy of 21.7% plagioclase, 34.8% amphibole, 30.5% garnet, 6.5% iron oxides, 2.2% pyroxene, and 4.3% olivine (mineralogies generated via MELTS using major element data to model equilibrium crystallization) underwent 5-20% fractional melting. When the resulting melt from the first fraction stage has undergone between 30-50% fractional crystallization in a second upper crustal fraction stage, the average Young Group composition can be approximately reconstructed, giving the theoretical petrogenetic evolution.

3.5 Discussion

Overall, trace element modeling suggests that the adakite-like characteristics of the El Valle Young group volcanic rocks can be produced via upper crustal fractional crystallization of partially melted lower crustal arc material. While there are no current radiometric ages for the biotite containing andesites, one could theorize that they are older than the non-biotite containing andesites, due to the higher SiO_2 content and lower MgO content, indicative of increased amount of crystallization in an arc system.

Modeling suggests that young group magmas formed via a two-stage process that includes: 1) lower crustal melting and 2) upper crustal fraction at depths similar to those modeled in the Coclé batholith using gravity data (Chapter 2). The partial melting of garnet bearing lower arc crustal material rather than subducting lithosphere agrees with the fact that modern geophysical data suggests a modern Benioff Zone does not exist beneath the southern boundary of the Panamá Block (e.g. Trenkamp et al. 2002). Subducted, altered basalt as was modeled and do not yield comparable results, therefore, it is suggested that the transition in magma signatures is not the result of melting of subducted oceanic lithosphere (e.g. Defant et al., 1991), continued fractionation of Old Group magmas, or a combination of the other scenarios paired with assimilation of the Old Group volcanics. Other modeled initial compositions failed to replicate enrichments in Sr as well as depletions heavy rare earth elements, which are typical of El Valle quaternary volcanics. In order to reproduce depletions in rare earth elements, the presence of garnet as a residual phase during melting was necessary, while the presence of hornblende was required during crystallization, due to the hydrous nature of pre-existing arc rocks at the lower crust modeled beneath El Valle. These necessities were met when the initial material used were mafic early arc rocks from the Kuna Yala. It is possible that a slab detachment occurred beneath Panamá; when this happened hot Galapagos plume material was supplied beneath El Valle and could have resulted in increased melting of the lower crust in Panamá (Figure 23). Western Panamá adakites, on a $^{206}Pb/^{204}Pb$ versus $^{207}Pb/^{204}Pb$ diagram, show compositions comparable to that of a Galapagos Island source (Abratis and Worner 2001). El Valle has similar $^{87}Sr/^{86}Sr$ and $^{143}Nd/^{144}Nd$ values to that of the Central American Arc; values that compare to arcs of the lowest radiogenic Sr and the highest radiogenic Nd (Defant et al. 1990). In contrast, Fowler et al. (2015) observed isotopic values for the Miocene arc that showed an increasing component of spreading center as the rocks approached El Valle from the Panamá Canal Basin. Additionally, the adakite

group samples have Sr and Nd isotopic ratios overlapping with those of a Galapagos Island source (Defant et al. 1992) consistent with the theory that Galapagos material being incorporated in the crust beneath El Valle, and playing a role in the petrogenetic of the Young Group rocks.

Previously there have been various hypotheses for the change in magma chemistries. Defant et al. (1991) proposed that the transition was due to melting of a young hot subducted slab. These geochemical models were based on the Young Group's adakite like characteristics, and utilized Sr and Y measurements rather than a full spectrum of trace elements. Goss and Kay (2006) proposed subduction erosion of the Cocos plate beneath Central America. The modeling was done using $^{206}Pb/^{204}Pb$ and $^{208}Pb/^{204}Pb$, however only one of the samples used was form El Valle. Abratis et al. (2001) suggested the cause could be due to slab-window processes, and not due to the melting of subducted material due to the Cocos Ridge being too old (15 Ma) and moving too fast (7-9 cm/yr) (Peacock et al., 1994). The upwelling Pacific mantle through the slab window may have allowed for melting of the Cocos Ridge by heating of the slab edge, facilitated by additional heat due to the highly oblique nature of subduction near Panamá. Rooney et al. (2015) has proposed the occurrence of oblique subduction as being responsible for the adakitic (Young Group) geochemical characteristic. After the late Miocene change in subduction obliquity, a more depleted and drier mantle wedge led to a decrease in the distribution and volume of magmatism in Panamá, apart from Quaternary adakitic-like lavas. Fluid-fluxed melting of the mantle wedge that is depleted due to the of asthenospheric flow due to continued oblique subduction. Some of the models proposed from authors (Abratis et al., 2001 & Rooney et al., 2015) are built upon the fact that oblique subduction is continuing in the Panamá region. However, geophysical evidence, including GPS and seismic data, suggest that a modern Benioff Zone does not exist beneath the southern boundary of the Panamá Block (e.g. Trenkamp et al. 2002). Hidalgo et al., 2010 determined the Young Groups geochemical signatures seen in El Valle are due to a two-stage fractionation model; with deep garnet fractionation coupled with mid crustal hornblende fractionation. The Hidalgo et al. (2010) El Valle geochemical models are similar to what is proposed here except they propose garnet present fractionation versus garnet present melting as is suggested here. On the basis of geochemical trace element modeling alone it is difficult to distinguish between the two models. However, it is suggested here that lower crustal melting above a slab window better fits existing geophysical observations suggesting a lack of subduction. Overall, while the melting and

crystallization of lower Panamá crust does correlate to geophysical data, it does not provide a definitive answer, but a non-unique solution that could provide insight into Panamá's magmatic evolution.
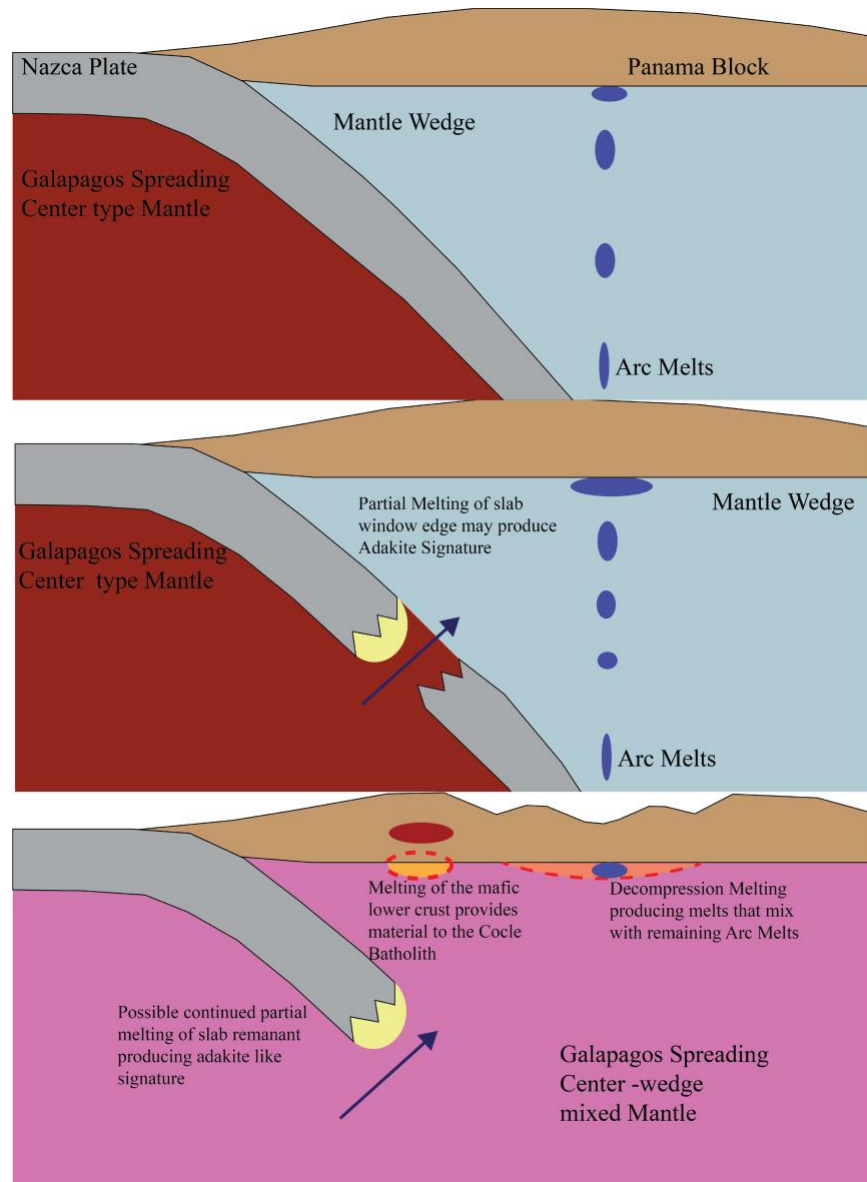
Figure 23: Schematic of the Panamá crust; showing the detachment of subducting crust, allowing for influx of Galapagos spreading center material and the melting of basal crustal material (figure modified from Fowler et al. 2017).

3.6 Conclusion

Eruptive products from the El Valle volcano are split into two groups, the Old Group, that are between 5-10 Ma, and the Young Group, which are <3Ma. These two groups have differing geochemical signatures, while both groups primarily plot in the calc-alkaline fields. The

Old Group volcanic rocks are relatively enriched in REE concentration, with a variation of major element trends and is predominantly andesitic. The Young Group displays depletions in REE, strong Sr/Y ratios, and enrichments in strontium while primarily consisting of dacite. Additional geologic mapping showed that there is a hydrous biotite-bearing andesitic sub-group within the Old group volcanic rocks that exhibit different geochemical trends, such as higher K_2O, from the previously described anhydrous andesite in the region. Fractional crystallization modeling suggests that the Young Group volcanics could be generated from the partial-melting and crystallization of Panamánian arc crust, which gave them their depleted HREE, Sr/Y and La/Yb ratios that are characteristic of these volcanics. This process could be due to the detachment of subducting crust underneath the Panamá crust, allowing for influx of mantle material. This influx of material and heat could have led to the melting of the lower crustal material that contained remnant pieces of the Caribbean crust, which would explain isotopic evidence for contributions from the Galapagos plume. Modal mineralogies calculated at crustal depths of 25 km and crystallization depths around 7 km provided starting compositions to be integrated with trace element compositions to calculate theoretical trace element signatures. Overall, geochemical models of the El Valle adakite-like rocks suggest a two-stage evolution, with an initial garnet-bearing lower crustal source that underwent 5-20% fractional melting, coupled with between of 30-50% upper crustal fractional crystallization.

CHAPTER 4

CONCLUSION

4.1 Integrated Conclusions From Both Gravity and Geochemical Observations

El Valle is the easternmost volcano in the Central American Volcanic Arc, and it's most recent volcanic activity is the eruption of the El Hato Ignimbrite. Both geophysical (gravity) and geochemical data and modeling thereof support the concept of a large sub-volcanic batholith beneath the El Valle volcanic complex. While the pyroclastic dacites have a lower density than the surrounding andesites, the regional low gravity anomaly observed in both satellite and terrestrial observations cannot be explained by their presence alone. Lithological and geophysical investigations conducted on the El Valle volcano suggest that the low gravity anomaly results from both subsurficial features along with surficial features. 2.5-dimensional gravity modeling completed using Talwani program suggest that the low density volcanics are between 0-2 kilometers thick, filling in the caldera features of El Valle, as well as blanketing the region, apart from extended coverage north of El Valle de Anton. In addition to the El Hato Ignimbrite, the gravity data suggest a large low-density feature located beneath the volcano, modeled as the Coclé Batholith. The batholith is located at 3-14 kilometers depth below El Valle and is about 35 kilometers long, 15 kilometers wide and 10 kilometers thick as implied by the gravity models. The modeled depths of the Coclé Batholith correlate to previously investigated magnesiohornblende geothermobarometry from magnesiohornblendes, which is consistent with the presence of a batholith in the proposed region. The combination of lithologic, geophysical, and geochemical data allows the placement and geometry of the Coclé Batholith underneath the El Valle volcano in central Panamá. The magma that resided in the Coclé Batholith helped shaped the region to what it is today.

In addition, new major and trace element geochemical data and modeling thereof, provide constraints on both the petrogenetic and geodynamic evolution of the El Valle volcano and the Miocene and younger evolution of the Panamánian subduction system. Volcanic rocks from El Valle can be divided into two groups, the Old Group that are between 5-10 Ma and the Young Group which are <3Ma; these two groups have differing geochemical signatures. Additional geologic mapping shows that there are hydrous biotite-bearing andesitic to dacitic Old group volcanic rocks that could have been emplaced after the eruption of the anhydrous Old group

andesites based of their silica content and MgO abundances. Fractional crystallization modeling suggests that the Young Group volcanics could have been generated in a two-stage process involving first melting of mafic lower crustal arc rocks followed by fractional crystallization in and the upper crust, likely within the Coclé batholith. Overall, such melting and crystallization, produced the unique depleted HREE, Sr/Y and La/Yb ratios that are characteristic of the Young Group volcanic rocks. In terms of geodynamic evolution of the Panamá arc, such a petrogenetic model supports the idea that slab break-off occurred between 5-10 Ma and that the resulting mantle upwelling induced partial melting of the Panamánian lower crust beneath the El Valle volcano.

APPENDIX A

DIFFERENTIAL GPS AND GRAVITY DATA

Table 2: Differential GPS and Gravity Data

Station Number	Latitude	Longitude	Elevation (MSL) EGM96	Absolute Gravity (mGal)	Calculated Gravity (sea level)	Free Air Gravity Correction	Bouguer Gravity Correction	Free-Air Anomaly (mGal)	Simple Bouguer Anomaly (mGal)
16EV001	8.560250	-79.944912	96.01	978149.454	978147.082	29.629	10.770	32.00	21.23
16EV002	8.600280	-79.888905	29.79	978173.500	978148.147	9.194	3.342	34.55	31.20
16EV003	8.604931	-79.795255	6.79	978187.831	978148.271	2.096	0.762	41.66	40.89
16EV004	8.519454	-79.904150	5.47	978177.045	978146.002	1.687	0.613	32.73	32.12
16EV005	8.527323	-79.914845	38.81	978167.609	978146.210	11.977	4.354	33.38	29.02
16EV006	8.537043	-79.920369	46.77	978164.317	978146.467	14.433	5.246	32.28	27.04
16EV007	8.546531	-79.911946	51.59	978161.279	978146.718	15.919	5.787	30.48	24.69
16EV008	8.550540	-79.926440	65.98	978155.953	978146.825	20.362	7.402	29.49	22.09
16EV009	8.554489	-79.940594	81.65	978153.590	978146.929	25.196	9.159	31.86	22.70
16EV010	8.560954	-79.949609	104.05	978147.969	978147.101	32.111	11.673	32.98	21.31
16EV011	8.566486	-79.961034	112.95	978144.137	978147.248	34.857	12.671	31.75	19.08
16EV012	8.568899	-79.973022	159.94	978131.663	978147.312	49.357	17.942	33.71	15.77
16EV013	8.571024	-79.985219	234.81	978108.605	978147.368	72.462	26.340	33.70	7.36
16EV014	8.582516	-79.992952	341.29	978080.862	978147.674	105.321	38.285	38.51	0.22
16EV015	8.586524	-80.006834	425.41	978050.411	978147.780	131.281	47.721	33.91	-13.81
16EV016	8.560250	-79.944906	95.83	978149.480	978147.082	29.573	10.750	31.97	21.22
16EV017	8.446143	-79.989138	30.27	978163.752	978144.074	9.340	3.395	29.02	25.62
16EV018	8.455004	-79.998593	50.28	978156.519	978144.306	15.515	5.640	27.73	22.09
16EV019	8.458272	-79.994129	49.29	978154.544	978144.392	15.210	5.529	25.36	19.83
16EV020	8.467203	-80.004402	69.43	978148.062	978144.626	21.425	7.788	24.86	17.07

Table 2: Continued

Station Number	Latitude	Longitude	Elevation (MSL) EGM96	Absolute Gravity (mGal)	Calculated Gravity (sea level)	Free Air Gravity Correction	Bouguer Gravity Correction	Free-Air Anomaly (mGal)	Simple Bouguer Anomaly (mGal)
16EV021	8.476950	-80.010730	85.08	978142.567	978144.882	26.255	9.544	23.94	14.40
16EV022	8.485527	-80.020238	98.33	978138.339	978145.108	30.345	11.030	23.58	12.55
16EV023	8.495974	-80.027740	128.77	978130.616	978145.383	39.737	14.445	24.97	10.53
16EV024	8.507839	-80.032722	182.35	978116.294	978145.696	56.272	20.455	26.87	6.41
16EV025	8.520198	-80.036893	235.97	978103.321	978146.022	72.820	26.470	30.12	3.65
16EV026	8.532315	-80.040506	290.03	978090.180	978146.342	89.502	32.534	33.34	0.81
16EV027	8.542720	-80.048925	351.07	978075.562	978146.617	108.341	39.383	37.29	-2.10
16EV028	8.552507	-80.055918	395.31	978063.839	978146.877	121.992	44.345	38.95	-5.39
16EV029	8.562573	-80.065212	485.78	978043.811	978147.144	149.910	54.493	46.58	-7.92
16EV030	8.317236	-80.205497	7.11	978178.285	978140.723	2.194	0.797	39.76	38.96
16EV031	8.328754	-80.210264	1.57	978176.251	978141.020	0.483	0.176	35.71	35.54
16EV032	8.341160	-80.214699	8.35	978175.323	978141.341	2.575	0.936	36.56	35.62
16EV033	8.354538	-80.220692	9.54	978173.939	978141.688	2.943	1.070	35.19	34.12
16EV034	8.367506	-80.225175	12.93	978172.867	978142.024	3.991	1.451	34.83	33.38
16EV035	8.379906	-80.228154	22.30	978170.841	978142.346	6.881	2.501	35.38	32.88
16EV036	8.396570	-80.231707	29.88	978168.292	978142.779	9.221	3.352	34.73	31.38
16EV037	8.399105	-80.265134	32.84	978167.491	978142.846	10.135	3.684	34.78	31.10
16EV038	8.409577	-80.260158	34.65	978165.026	978143.118	10.693	3.887	32.60	28.71
16EV039	8.423820	-80.258259	49.25	978160.865	978143.490	15.197	5.524	32.57	27.05
16EV040	8.436607	-80.257991	55.38	978158.333	978143.824	17.089	6.212	31.60	25.39
16EV041	8.449981	-80.254525	63.32	978156.265	978144.175	19.541	7.103	31.63	24.53
16EV042	8.462768	-80.251738	75.96	978160.004	978144.510	23.442	8.521	38.94	30.41
16EV043	8.475362	-80.246713	91.63	978149.429	978144.841	28.276	10.278	32.86	22.59
16EV044	8.483014	-80.236949	114.96	978143.909	978145.042	35.476	12.896	34.34	21.45

Table 2: Continued

Station Number	Latitude	Longitude	Elevation (MSL) EGM96	Absolute Gravity (mGal)	Calculated Gravity (sea level)	Free Air Gravity Correction	Bouguer Gravity Correction	Free-Air Anomaly (mGal)	Simple Bouguer Anomaly (mGal)
16EV045	8.494203	-80.228324	139.68	978137.993	978145.336	43.105	15.669	35.76	20.09
16EV046	8.505114	-80.223849	162.80	978132.397	978145.624	50.240	18.263	37.01	18.75
16EV047	8.515973	-80.215243	178.66	978128.202	978145.910	55.134	20.041	37.43	17.38
16EV048	8.526209	-80.208372	246.09	978113.162	978146.181	75.942	27.605	42.92	15.32
16EV049	8.536603	-80.201498	278.51	978106.174	978146.455	85.949	31.243	45.67	14.42
16EV050	8.545813	-80.196915	310.77	978098.443	978146.699	95.903	34.861	47.65	12.79
16EV051	8.555846	-80.191323	353.45	978086.661	978146.965	109.075	39.650	48.77	9.12
16EV052	8.562422	-80.182294	419.87	978070.110	978147.140	129.573	47.101	52.54	5.44
16EV053	8.572988	-80.172890	498.69	978047.178	978147.420	153.896	55.942	53.65	-2.29
16EV055	8.560265	-79.944899	98.45	978149.404	978147.082	30.381	11.044	32.70	21.66
16EV056	8.398017	-80.190398	41.11	978167.284	978142.817	12.685	4.611	37.15	32.54
16EV057	8.410546	-80.189203	49.27	978165.807	978143.144	15.205	5.527	37.87	32.34
16EV058	8.423661	-80.185694	64.97	978159.333	978143.486	20.049	7.288	35.90	28.61
16EV059	8.437610	-80.183284	84.64	978151.915	978143.851	26.119	9.495	34.18	24.69
16EV060	8.450988	-80.181937	98.32	978146.817	978144.201	30.341	11.029	32.96	21.93
16EV061	8.467228	-80.183601	124.52	978141.694	978144.627	38.427	13.968	35.49	21.53
16EV062	8.482117	-80.181611	152.12	978135.718	978145.018	46.944	17.064	37.64	20.58
16EV063	8.493886	-80.185466	185.28	978130.215	978145.328	57.176	20.784	42.06	21.28
16EV064	8.505219	-80.182406	183.30	978129.473	978145.626	56.566	20.562	40.41	19.85
16EV065	8.512996	-80.180185	230.45	978117.083	978145.832	71.116	25.851	42.37	16.52
16EV066	8.524957	-80.177753	277.91	978108.330	978146.148	85.762	31.175	47.95	16.77
16EV067	8.533662	-80.171065	318.24	978098.979	978146.378	98.207	35.699	50.81	15.11
16EV068	8.540625	-80.169644	360.94	978087.897	978146.562	111.387	40.490	52.72	12.23
16EV069	8.549068	-80.161184	432.62	978068.359	978146.786	133.507	48.531	55.08	6.55

Table 2: Continued

Station Number	Latitude	Longitude	Elevation (MSL) EGM96	Absolute Gravity (mGal)	Calculated Gravity (sea level)	Free Air Gravity Correction	Bouguer Gravity Correction	Free-Air Anomaly (mGal)	Simple Bouguer Anomaly (mGal)
16EV070	8.560198	-80.157142	492.11	978051.251	978147.081	151.865	55.204	56.03	0.83
16EV071	8.564833	-80.154953	503.91	978047.267	978147.204	155.508	56.528	55.57	-0.96
16EV072	8.402493	-80.057383	3.97	978167.090	978142.934	1.226	0.446	25.38	24.94
16EV073	8.414695	-80.062957	48.77	978153.552	978143.252	15.050	5.471	25.35	19.88
16EV074	8.427106	-80.070273	67.52	978148.505	978143.576	20.838	7.575	25.77	18.19
16EV075	8.438945	-80.076182	84.67	978143.669	978143.886	26.128	9.498	25.91	16.41
16EV076	8.451671	-80.080249	109.75	978139.415	978144.219	33.868	12.311	29.06	16.75
16EV077	8.461786	-80.088628	133.62	978135.043	978144.484	41.234	14.989	31.79	16.80
16EV078	8.474353	-80.095204	171.85	978126.907	978144.814	53.032	19.277	35.12	15.85
16EV079	8.486534	-80.099921	204.93	978119.556	978145.134	63.241	22.988	37.66	14.67
16EV080	8.516994	-80.352649	87.34	978154.742	978145.937	26.952	9.797	35.76	25.96
16EV081	8.527536	-80.346559	95.98	978154.396	978146.216	29.618	10.766	37.80	27.03
16EV082	8.539542	-80.342935	100.29	978153.240	978146.533	30.949	11.250	37.65	26.40
16EV083	8.545193	-80.332620	92.81	978151.062	978146.683	28.642	10.411	33.02	22.61
16EV084	8.557001	-80.326470	88.17	978154.227	978146.996	27.208	9.890	34.44	24.55
16EV085	8.558563	-80.313413	108.18	978149.467	978147.037	33.385	12.136	35.81	23.68
16EV086	8.562473	-80.301636	116.96	978146.808	978147.141	36.094	13.120	35.76	22.64
16EV087	8.566185	-80.287962	151.18	978138.301	978147.240	46.654	16.959	37.72	20.76
16EV088	8.573008	-80.277060	170.53	978131.734	978147.421	52.625	19.129	36.94	17.81
16EV089	8.580310	-80.275430	146.94	978137.305	978147.615	45.346	16.483	35.04	18.55
16EV090	8.594986	-80.273995	192.14	978126.122	978148.006	59.294	21.554	37.41	15.86
16EV091	8.608837	-80.265798	213.06	978119.454	978148.375	65.751	23.901	36.83	12.93
16EV092	8.617861	-80.251396	238.33	978106.870	978148.616	73.547	26.735	31.80	5.07
16EV093	8.626077	-80.235886	279.11	978097.949	978148.835	86.133	31.310	35.25	3.94

Table 2: Continued

Station Number	Latitude	Longitude	Elevation (MSL) EGM96	Absolute Gravity (mGal)	Calculated Gravity (sea level)	Free Air Gravity Correction	Bouguer Gravity Correction	Free-Air Anomaly (mGal)	Simple Bouguer Anomaly (mGal)
16EV094	8.635773	-80.223596	329.55	978079.921	978149.094	101.699	36.968	32.53	-4.44
16EV095	8.654337	-80.204436	359.77	978077.136	978149.592	111.026	40.359	38.57	-1.79
16EV096	8.584098	-80.267687	187.62	978127.565	978147.716	57.900	21.047	37.75	16.70
16EV097	8.586451	-80.259441	199.69	978124.020	978147.778	61.624	22.401	37.87	15.47
16EV098	8.562063	-80.275803	162.89	978134.266	978147.130	50.266	18.272	37.40	19.13
16EV099	8.554308	-80.267764	159.86	978132.857	978146.924	49.331	17.932	35.26	17.33
16EV100	8.554078	-80.255956	205.00	978124.670	978146.918	63.262	22.996	41.01	18.02
16EV101	8.556716	-80.248575	204.28	978123.657	978146.988	63.040	22.916	39.71	16.79
16EV102	8.551318	-80.238425	222.19	978117.522	978146.845	68.566	24.924	39.24	14.32
16EV103	8.554863	-80.223692	265.34	978107.647	978146.939	81.883	29.765	42.59	12.83
16EV104	8.563185	-80.216119	282.06	978100.194	978147.160	87.043	31.641	40.08	8.44
16EV105	8.572839	-80.206785	325.56	978084.707	978147.416	100.466	36.520	37.76	1.24
16EV106	8.581647	-80.194531	452.59	978053.310	978147.650	139.668	50.770	45.33	-5.44
16EV107	8.555031	-80.059453	430.97	977948.262	978146.944	132.996	48.345	-65.69	-114.03
16EV108	8.569026	-80.073029	546.29	978032.079	978147.315	168.584	61.281	53.35	-7.93
16EV109	8.581300	-80.077612	598.70	978022.466	978147.641	184.758	67.161	59.58	-7.58
16EV110	8.587666	-80.084875	697.67	978000.530	978147.811	215.302	78.264	68.02	-10.24
16EV111	8.593130	-80.084457	728.73	977993.821	978147.956	224.885	81.747	70.75	-11.00
16EV112	8.598348	-80.089974	730.19	977995.357	978148.095	225.335	81.911	72.60	-9.31
16EV113	8.600930	-80.096356	698.56	978004.008	978148.164	215.576	78.363	71.42	-6.94
16EV114	8.599981	-80.100402	736.40	977996.083	978148.139	227.253	82.608	75.20	-7.41
16EV115	8.592485	-80.105955	726.38	977999.214	978147.939	224.162	81.484	75.44	-6.05
16EV116	8.595479	-80.110201	643.61	978018.356	978148.019	198.619	72.199	68.96	-3.24
16EV117	8.598120	-80.116013	590.40	978027.868	978148.089	182.197	66.230	61.98	-4.25

Table 2: Continued

Station Number	Latitude	Longitude	Elevation (MSL) EGM96	Absolute Gravity (mGal)	Calculated Gravity (sea level)	Free Air Gravity Correction	Bouguer Gravity Correction	Free-Air Anomaly (mGal)	Simple Bouguer Anomaly (mGal)
16EV118	8.604353	-80.123669	585.65	978025.336	978148.255	180.731	65.697	57.81	-7.89
16EV119	8.605159	-80.133421	582.48	978026.559	978148.277	179.754	65.342	58.04	-7.31
16EV120	8.605295	-80.140511	583.82	978028.408	978148.280	180.166	65.491	60.29	-5.20
16EV121	8.598985	-80.147007	588.63	978029.125	978148.112	181.650	66.031	62.66	-3.37
16EV122	8.594803	-80.146770	585.35	978029.100	978148.001	180.638	65.663	61.74	-3.93
16EV123	8.595996	-80.150995	667.30	978010.388	978148.032	205.929	74.857	68.29	-6.57
16EV124	8.594404	-80.154887	777.06	977984.258	978147.990	239.799	87.169	76.07	-11.10
16EV125	8.587773	-80.156995	680.88	978004.658	978147.813	210.120	76.380	66.96	-9.42
16EV126	8.581462	-80.161869	609.43	978020.778	978147.646	188.070	68.365	61.20	-7.16
16EV127	8.572974	-80.172902	498.27	978047.448	978147.420	153.767	55.895	53.80	-2.10
16EV128	8.565500	-80.177561	453.35	978062.438	978147.221	139.904	50.856	55.12	4.26
16EV129	8.595297	-80.161932	686.72	978005.611	978148.014	211.921	77.034	69.52	-7.52
16EV130	8.592592	-80.170585	593.84	978024.061	978147.942	183.257	66.615	59.38	-7.24
16EV131	8.591099	-80.178566	551.27	978032.560	978147.902	170.122	61.840	54.78	-7.06
16EV132	8.583672	-80.190141	478.02	978049.060	978147.704	147.518	53.624	48.87	-4.75
16EV133	8.578669	-80.198394	415.27	978063.214	978147.571	128.151	46.584	43.79	-2.79
16EV134	8.599976	-80.137364	577.90	978022.217	978148.138	178.339	64.827	52.42	-12.41
16EV135	8.599310	-80.132438	579.29	978028.243	978148.121	178.770	64.984	58.89	-6.09
16EV136	8.599340	-80.127441	579.77	978028.024	978148.122	178.918	65.038	58.82	-6.22
16EV137	8.598240	-80.122960	583.09	978028.370	978148.092	179.942	65.410	60.22	-5.19
16EV138	8.595211	-80.121091	587.88	978029.163	978148.012	181.420	65.947	62.57	-3.38
16EV139	8.599196	-80.120125	587.29	978027.998	978148.118	181.237	65.881	61.12	-4.76
16EV140	8.602543	-80.118478	591.14	978025.720	978148.207	182.426	66.313	59.94	-6.37
16EV141	8.607119	-80.116156	599.15	978032.581	978148.329	184.898	67.212	69.15	1.94

Table 2: Continued

Station Number	Latitude	Longitude	Elevation (MSL) EGM96	Absolute Gravity (mGal)	Calculated Gravity (sea level)	Free Air Gravity Correction	Bouguer Gravity Correction	Free-Air Anomaly (mGal)	Simple Bouguer Anomaly (mGal)
16EV142	8.612352	-80.113581	617.20	978022.158	978148.469	190.469	69.237	64.16	-5.08
16EV143	8.617016	-80.110960	657.39	978014.321	978148.593	202.869	73.744	68.60	-5.15
16EV144	8.619401	-80.107265	676.75	978011.823	978148.657	208.846	75.917	72.01	-3.90
16EV145	8.620326	-80.102336	753.56	977996.412	978148.681	232.548	84.533	80.28	-4.25
16EV146	8.621661	-80.096927	709.58	978006.658	978148.717	218.976	79.599	76.92	-2.68
16EV147	8.611531	-80.115783	612.50	978021.757	978148.447	189.018	68.709	62.33	-6.38
16EV148	8.612783	-80.120023	620.18	978011.764	978148.480	191.387	69.570	54.67	-14.90
16EV149	8.612253	-80.125144	605.96	978023.369	978148.466	186.998	67.975	61.90	-6.07
16EV150	8.615434	-80.133320	601.66	978026.585	978148.551	185.673	67.493	63.71	-3.79
16EV151	8.610789	-80.134121	592.81	978025.977	978148.427	182.941	66.500	60.49	-6.01
16EV152	8.605802	-80.136651	582.11	978027.091	978148.294	179.639	65.300	58.44	-6.86
16EV153	8.598018	-80.137697	575.38	978028.712	978148.086	177.563	64.545	58.19	-6.36
16EV154	8.594636	-80.129408	597.69	978027.302	978147.996	184.446	67.047	63.75	-3.30
16EV155	8.603390	-80.128637	582.21	978026.534	978148.229	179.668	65.311	57.97	-7.34
16EV156	8.607524	-80.126308	589.54	978026.492	978148.340	181.932	66.134	60.08	-6.05
16EV157	8.613163	-80.144742	608.02	978025.884	978148.490	187.634	68.206	65.03	-3.18
16EV158	8.609053	-80.146246	595.33	978026.770	978148.381	183.719	66.783	62.11	-4.67
16EV159	8.604533	-80.147174	591.28	978033.793	978148.260	182.470	66.329	68.00	1.67
16EV160	8.606401	-80.112913	603.48	978024.365	978148.310	186.235	67.697	62.29	-5.41
16EV161	8.599930	-80.112834	607.40	978034.096	978148.137	187.445	68.137	73.40	5.27
16EV162	8.586530	-80.006832	423.39	978050.348	978147.780	130.658	47.495	33.22	-14.27
16EV163	8.592319	-80.017302	525.70	978025.416	978147.934	162.230	58.972	39.71	-19.26
16EV164	8.597494	-80.029251	501.61	978031.678	978148.072	154.797	56.270	38.40	-17.87
16EV165	8.597134	-80.037324	582.88	978013.245	978148.063	179.876	65.386	45.06	-20.33

Table 2: Continued

Station Number	Latitude	Longitude	Elevation (MSL) EGM96	Absolute Gravity (mGal)	Calculated Gravity (sea level)	Free Air Gravity Correction	Bouguer Gravity Correction	Free-Air Anomaly (mGal)	Simple Bouguer Anomaly (mGal)
16EV166	8.607434	-80.040971	599.21	978011.169	978148.337	184.917	67.219	47.75	-19.47
16EV167	8.608578	-80.049353	632.72	978005.185	978148.368	195.256	70.977	52.07	-18.90
16EV168	8.620876	-80.055544	757.43	977982.448	978148.696	233.743	84.967	67.49	-17.47
16EV169	8.625149	-80.050128	778.35	977976.143	978148.810	240.198	87.313	67.53	-19.78
16EV170	8.652860	-80.032365	783.15	977975.240	978149.552	241.680	87.852	67.37	-20.48
16EV171	8.644980	-80.019584	669.25	977997.851	978149.341	206.531	75.075	55.04	-20.03
16EV172	8.636155	-80.009889	544.52	978027.374	978149.105	168.038	61.083	46.31	-14.78
16EV173	8.639071	-79.997042	396.42	978061.784	978149.183	122.335	44.470	34.94	-9.53
16EV174	8.638567	-80.002956	468.96	978044.676	978149.169	144.722	52.607	40.23	-12.38
16EV175	8.639548	-79.988891	385.91	978064.333	978149.195	119.092	43.291	34.23	-9.06
16EV176	8.640324	-79.978592	328.26	978078.689	978149.216	101.301	36.823	30.77	-6.05
16EV177	8.648021	-79.941324	422.24	978070.827	978149.422	130.304	47.366	51.71	4.34
16EV178	8.661058	-79.938710	538.17	978049.651	978149.772	166.080	60.371	65.96	5.59
16EV179	8.669571	-79.932921	668.49	978024.019	978150.001	206.294	74.989	80.31	5.32
16EV180	8.670113	-79.926993	762.35	978004.565	978150.015	235.262	85.519	89.81	4.29
16EV181	8.678624	-79.923242	814.12	977992.951	978150.244	251.237	91.326	93.94	2.62
16EV182	8.688881	-79.916188	618.81	978037.093	978150.520	190.965	69.417	77.54	8.12
16EV183	8.691626	-79.907577	603.40	978040.646	978150.594	186.210	67.688	76.26	8.57
16EV184	8.701102	-79.901712	470.36	978069.359	978150.849	145.154	52.764	63.66	10.90
16EV185	8.704300	-79.896286	400.58	978085.150	978150.935	123.620	44.937	57.83	12.90
16EV186	8.708152	-79.885577	235.92	978120.986	978151.039	72.803	26.464	42.75	16.29
16EV187	8.712114	-79.879891	192.59	978130.853	978151.146	59.434	21.605	39.14	17.54
16EV188	8.600310	-79.888899	29.83	978173.719	978148.147	9.204	3.346	34.78	31.43
16EV189	8.609939	-79.899494	20.63	978175.846	978148.404	6.367	2.314	33.81	31.49

Table 2: Continued

Station Number	Latitude	Longitude	Elevation (MSL) EGM96	Absolute Gravity (mGal)	Calculated Gravity (sea level)	Free Air Gravity Correction	Bouguer Gravity Correction	Free-Air Anomaly (mGal)	Simple Bouguer Anomaly (mGal)
16EV190	8.620425	-79.909959	36.89	978172.614	978148.684	11.383	4.138	35.31	31.17
16EV191	8.624163	-79.922022	44.57	978170.234	978148.784	13.756	5.000	35.21	30.20
16EV192	8.629697	-79.934027	70.89	978157.379	978148.932	21.876	7.952	30.32	22.37
16EV193	8.632226	-79.945788	211.67	978120.395	978149.000	65.321	23.745	36.72	12.97
16EV194	8.634896	-79.949343	190.29	978124.860	978149.071	58.724	21.346	34.51	13.17
16EV195	8.639820	-79.960519	92.09	978141.192	978149.203	28.420	10.331	20.41	10.08
16EV196	8.643463	-79.970152	211.03	978116.597	978149.300	65.123	23.672	32.42	8.75
16EV197	8.718306	-79.753712	3.09	978160.494	978151.313	0.955	0.347	10.14	9.79
16EV198	8.713927	-79.765398	9.53	978161.743	978151.195	2.942	1.069	13.49	12.42
16EV199	8.717346	-79.771276	40.34	978156.088	978151.287	12.449	4.525	17.25	12.72
16EV200	8.721242	-79.784554	25.79	978164.157	978151.393	7.960	2.894	20.72	17.83
16EV201	8.731304	-79.794907	9.78	978169.601	978151.665	3.018	1.097	20.95	19.86
16EV202	8.732940	-79.806716	31.43	978164.047	978151.709	9.700	3.526	22.04	18.51
16EV203	8.739571	-79.813028	50.91	978158.620	978151.888	15.711	5.711	22.44	16.73
16EV204	8.741420	-79.829018	236.30	978119.205	978151.938	72.922	26.507	40.19	13.68
16EV205	8.741799	-79.844308	207.39	978122.261	978151.949	64.001	23.265	34.31	11.05
16EV206	8.747413	-79.856615	140.66	978135.621	978152.101	43.406	15.778	26.93	11.15
16EV207	8.758525	-79.870002	103.73	978143.141	978152.402	32.011	11.636	22.75	11.11
16EV208	8.757009	-79.879753	108.09	978140.432	978152.361	33.357	12.126	21.43	9.30
16EV209	8.752304	-79.895219	105.47	978139.681	978152.233	32.547	11.831	19.99	8.16
16EV210	8.746849	-79.910730	122.97	978134.912	978152.085	37.949	13.795	20.78	6.98
16EV211	8.746241	-79.925842	148.65	978128.658	978152.069	45.873	16.675	22.46	5.79
16EV212	8.748866	-79.943625	286.94	978099.422	978152.140	88.549	32.188	35.83	3.64
16EV213	8.747627	-79.959563	468.36	978060.556	978152.106	144.536	52.540	52.99	0.45

Table 2: Continued

Station Number	Latitude	Longitude	Elevation (MSL) EGM96	Absolute Gravity (mGal)	Calculated Gravity (sea level)	Free Air Gravity Correction	Bouguer Gravity Correction	Free-Air Anomaly (mGal)	Simple Bouguer Anomaly (mGal)
16EV214	8.741411	-79.974289	389.02	978076.339	978151.938	120.050	43.639	44.45	0.81
16EV215	8.745950	-79.990476	202.37	978114.555	978152.061	62.452	22.702	24.95	2.24
16EV216	8.856730	-79.879056	94.78	978153.320	978155.081	29.250	10.633	27.49	16.86
16EV217	8.844105	-79.891265	84.04	978153.472	978154.735	25.933	9.427	24.67	15.24
16EV218	8.840606	-79.910507	128.45	978147.049	978154.639	39.641	14.410	32.05	17.64
16EV219	8.841178	-79.927644	203.27	978131.950	978154.654	62.728	22.802	40.02	17.22
16EV220	8.845094	-79.942330	166.51	978142.407	978154.762	51.385	18.679	39.03	20.35
16EV221	8.844362	-79.939133	167.60	978157.831	978154.742	51.721	18.801	54.81	36.01
16EV222	8.847901	-79.957567	211.08	978150.919	978154.839	65.140	23.679	61.22	37.54
16EV223	8.858498	-79.971301	268.77	978144.639	978155.129	82.943	30.150	72.45	42.30
16EV224	8.871236	-79.981632	239.54	978153.012	978155.479	73.922	26.871	71.45	44.58
16EV225	8.868884	-79.998214	101.69	978185.160	978155.414	31.381	11.407	61.13	49.72
16EV226	8.866035	-80.014727	303.78	978144.023	978155.336	93.745	34.077	82.43	48.36
16EV227	8.867022	-80.030819	213.23	978161.528	978155.363	65.802	23.920	71.97	48.05
16EV228	8.866521	-80.045679	127.83	978178.728	978155.349	39.447	14.339	62.83	48.49
16EV229	8.860239	-80.058618	140.70	978174.500	978155.177	43.419	15.783	62.74	46.96
16EV230	8.857386	-80.071219	226.74	978156.413	978155.099	69.973	25.436	71.29	45.85
16EV231	8.939259	-79.908025	154.25	978184.079	978157.354	47.601	17.303	74.33	57.02
16EV232	8.937185	-79.922192	142.54	978190.781	978157.297	43.987	15.989	77.47	61.48
16EV233	8.941142	-79.939294	207.63	978176.365	978157.406	64.075	23.292	83.03	59.74
16EV234	8.951100	-79.952771	148.04	978188.181	978157.682	45.684	16.606	76.18	59.58
16EV235	8.970789	-79.968922	99.32	978195.617	978158.228	30.649	11.141	68.04	56.90
16EV236	8.935922	-79.905447	159.72	978182.999	978157.262	49.289	17.917	75.03	57.11
16EV237	8.945391	-79.899792	146.89	978187.118	978157.524	45.330	16.478	74.92	58.45

Table 2: Continued

Station Number	Latitude	Longitude	Elevation (MSL) EGM96	Absolute Gravity (mGal)	Calculated Gravity (sea level)	Free Air Gravity Correction	Bouguer Gravity Correction	Free-Air Anomaly (mGal)	Simple Bouguer Anomaly (mGal)
16EV238	9.020314	-79.895080	55.85	978212.725	978159.607	17.235	6.265	70.35	64.09
16EV239	9.015658	-79.876152	119.76	978191.304	978159.477	36.957	13.434	68.78	55.35
16EV240	9.013180	-79.849390	138.60	978185.075	978159.408	42.773	15.548	68.44	52.89
16EV241	8.990512	-79.847853	79.79	978200.217	978158.776	24.624	8.951	66.06	57.11
16EV242	8.965918	-79.838556	116.47	978188.375	978158.093	35.944	13.066	66.23	53.16
16EV243	8.948108	-79.822243	100.94	978185.826	978157.599	31.150	11.323	59.38	48.05
16EV244	8.936891	-79.808813	97.08	978184.594	978157.288	29.960	10.890	57.27	46.37
16EV245	8.925379	-79.802731	106.54	978181.286	978156.970	32.878	11.951	57.19	45.24
16EV246	8.912208	-79.794040	71.97	978186.611	978156.607	22.209	8.073	52.21	44.14
16EV247	8.895632	-79.790285	37.45	978184.113	978156.150	11.557	4.201	39.52	35.32
16EV248	8.942675	-79.679680	69.98	978211.868	978157.448	21.595	7.850	76.01	68.16
16EV249	8.954851	-79.689843	45.22	978216.789	978157.786	13.954	5.072	72.96	67.88
16EV250	8.967459	-79.700824	92.67	978204.795	978158.135	28.597	10.395	75.26	64.86
16EV251	8.980331	-79.710040	125.39	978197.275	978158.493	38.697	14.066	77.48	63.41
16EV252	8.994449	-79.722733	119.86	978197.815	978158.886	36.989	13.446	75.92	62.47
16EV253	9.007504	-79.732869	115.67	978200.871	978159.249	35.695	12.975	77.32	64.34
16EV254	9.023237	-79.740224	147.65	978195.157	978159.688	45.564	16.563	81.03	64.47
16EV255	9.037378	-79.750409	95.31	978207.243	978160.083	29.413	10.692	76.57	65.88
16EV256	9.037433	-79.739621	86.97	978209.091	978160.085	26.840	9.757	75.85	66.09
16EV257	9.036244	-79.755724	132.33	978199.976	978160.052	40.837	14.845	80.76	65.92
16EV258	9.002576	-79.730970	121.89	978198.643	978159.112	37.614	13.673	77.14	63.47
16EV259	8.996105	-79.745778	113.36	978197.883	978158.932	34.984	12.717	73.94	61.22
16EV260	8.981329	-79.754168	110.60	978195.267	978158.521	34.130	12.406	70.88	58.47
16EV261	8.965430	-79.757050	120.82	978189.384	978158.079	37.284	13.553	68.59	55.04

Table 2: Continued

Station Number	Latitude	Longitude	Elevation (MSL) EGM96	Absolute Gravity (mGal)	Calculated Gravity (sea level)	Free Air Gravity Correction	Bouguer Gravity Correction	Free-Air Anomaly (mGal)	Simple Bouguer Anomaly (mGal)
16EV262	8.952207	-79.762344	114.53	978187.333	978157.712	35.345	12.848	64.97	52.12
16EV263	8.939746	-79.772868	94.46	978188.017	978157.367	29.150	10.596	59.80	49.20
16EV264	8.924667	-79.777563	66.08	978190.321	978156.951	20.392	7.413	53.76	46.35
16EV265	8.907678	-79.782894	62.98	978188.464	978156.482	19.434	7.065	51.42	44.35
16EV266	8.892003	-79.778540	67.02	978184.928	978156.050	20.681	7.518	49.56	42.04
16EV267	8.911063	-79.568480	51.31	978208.222	978156.575	15.836	5.756	67.48	61.73
16EV268	8.902884	-79.572787	12.72	978214.856	978156.349	3.925	1.427	62.43	61.00
16EV269	8.900645	-79.583144	10.13	978213.455	978156.288	3.126	1.136	60.29	59.16
16EV270	8.894736	-79.586250	21.15	978208.399	978156.125	6.526	2.372	58.80	56.43
16EV271	8.892981	-79.589125	25.94	978206.652	978156.077	8.004	2.910	58.58	55.67
16EV272	8.893462	-79.596308	4.75	978210.543	978156.090	1.466	0.533	55.92	55.39
16EV273	8.894026	-79.599280	5.05	978210.172	978156.105	1.559	0.567	55.63	55.06
16EV274	8.894747	-79.604445	5.15	978210.400	978156.125	1.589	0.578	55.86	55.29
16EV275	8.894522	-79.607619	4.25	978210.298	978156.119	1.312	0.477	55.49	55.01

APPENDIX B

MAJOR ELEMENT GEOCHEMICAL ANALYSES

Table 3: Major element geochemical analyses, values reported in weight percent.

Sample ID	SiO_2	TiO_2	Al_2O_3	Fe_2O_3	Cr_2O_3	$FeO_{(Total)}$	MnO	MgO
16EV013	71.21	0.40	14.39	5.26	<0.01	4.73	0.09	0.48
16EV014	60.80	0.46	17.26	7.76	<0.01	6.98	0.13	2.83
16EV017	66.21	0.24	16.30	5.03	0.01	4.53	0.09	0.86
16EV070A	59.28	0.59	17.38	7.27	<0.01	6.54	0.17	3.23
16EV070B	67.60	0.27	16.32	5.25	<0.01	4.72	0.10	1.20
16EV070D	66.35	0.25	15.78	3.97	<0.01	3.57	0.08	1.04
16EV084	65.70	0.47	15.30	5.68	<0.01	5.11	0.08	1.04
16EV089	66.60	0.47	15.22	4.32	<0.01	3.89	0.08	1.11

Sample ID	CaO	Na_2O	K_2O	P_2O_5	Total	LOI 1000
16EV013	1.82	2.33	2.20	0.01	100.10	1.70
16EV014	4.61	3.20	0.94	0.16	99.01	0.63
16EV017	3.62	3.90	1.80	0.09	100.25	1.81
16EV070A	6.93	3.37	1.18	0.15	100.25	0.48
16EV070B	4.47	4.20	1.33	0.11	100.45	-0.61
16EV070D	3.90	3.64	1.57	0.10	99.84	2.94
16EV084	3.11	3.47	3.71	0.14	98.82	-0.18
16EV089	3.12	3.19	4.00	0.14	99.35	0.74

Table 3: Continued

Sample ID	SiO$_2$	TiO$_2$	Al$_2$O$_3$	Fe$_2$O$_3$	Cr$_2$O$_3$	FeO$_{(Total)}$	MnO	MgO
16EV099	66.39	0.46	15.02	5.93	<0.01	5.34	0.10	1.06
16EV101	66.54	0.47	15.15	4.58	<0.01	4.12	0.10	1.20
16EV103A	68.20	0.42	14.66	5.08	<0.01	4.57	0.06	0.82
16EV103B	66.21	0.23	16.55	3.84	<0.01	3.46	0.08	0.90
16EV124	65.74	0.26	16.74	5.10	<0.01	4.59	0.10	1.14
16EV164	60.97	0.55	17.41	6.55	<0.01	5.89	0.09	2.19
16EV166	52.93	0.78	18.04	9.55	0.01	8.59	0.16	4.74
16EV169	59.73	0.53	17.22	7.01	0.01	6.31	0.20	3.41
16EV171	61.72	0.50	17.14	6.87	<0.01	6.18	0.11	2.77
16EV173	56.65	1.38	14.68	10.42	<0.01	9.38	0.23	3.32
16EV176	58.39	0.62	17.72	7.70	<0.01	6.93	0.11	3.71
16EV283	66.30	0.30	16.92	4.23	<0.01	3.81	0.09	1.24

Sample ID	CaO	Na$_2$O	K$_2$O	P$_2$O$_5$	Total	LOI 1000
16EV099	3.04	3.14	4.03	0.13	99.91	0.24
16EV101	3.35	3.25	4.00	0.14	100.10	1.00
16EV103A	2.51	3.27	4.28	0.11	99.68	0.00
16EV103B	3.66	3.93	1.49	0.10	99.91	2.67
16EV124	3.87	4.05	1.35	0.11	98.90	0.23
16EV164	5.46	3.64	1.29	0.22	99.16	0.56
16EV166	8.93	3.09	0.56	0.20	99.12	-0.07
16EV169	6.93	3.54	1.16	0.20	100.35	0.16
16EV171	5.49	3.49	1.18	0.17	99.98	0.33
16EV173	6.67	3.62	1.37	0.45	98.96	-0.08
16EV176	6.68	3.21	0.95	0.15	100.05	0.62
16EV283	3.36	3.68	1.31	0.12	99.38	1.62

Table 3: Continued

Sample ID	SiO$_2$	TiO$_2$	Al$_2$O$_3$	Fe$_2$O$_3$	Cr$_2$O$_3$	FeO$_{(Total)}$	MnO	MgO
16EV284	64.83	0.27	17.76	4.34	<0.01	3.91	0.09	1.20
16EV286	57.84	0.60	17.86	7.05	<0.01	6.34	0.10	3.69
16EV287	67.23	0.23	16.69	3.71	<0.01	3.34	0.07	0.96
16EV288	65.65	0.31	16.64	4.09	<0.01	3.68	0.08	0.91
16EV291A	65.78	0.75	15.14	5.57	<0.01	5.01	0.09	0.84
16EV291B	66.54	0.70	14.86	4.10	<0.01	3.69	0.09	0.74
NCSDC73303	44.49	2.37	13.86	13.40	0.02		0.17	7.65
OREAS-13B	48.69	1.17	15.92	12.02	1.58		0.16	5.11

Sample ID	CaO	Na$_2$O	K$_2$O	P$_2$O$_5$	Total	LOI 1000
16EV284	3.32	3.49	1.28	0.11	99.34	2.46
16EV286	6.95	3.19	0.86	0.15	99.33	0.85
16EV287	4.14	4.54	1.54	0.1	100.25	0.81
16EV288	4.18	3.52	1.49	0.14	99.64	2.4
16EV291A	3.45	3.53	3.17	0.18	99.45	0.61
16EV291B	2.67	3.61	3.78	0.15	98.82	1.3
NCSDC73303	8.86	3.36	2.33	0.96	100.10	
OREAS-13B	7.72	2.27	2.76	0.42	101.55	

APPENDIX C

TRACE ELEMENT GEOCHEMICAL ANALYSES

Table 4: Trace element geochemical analyses reported in parts per million.

Sample ID	Cs	Rb	Ba	Th	Nb	Ta	La	Ce	Sr
16EV013	1.76	106.86	1906	4.86	13.11	0.89	22.54	38.5	441
16EV014	0.68	23.00	2082	2.39	6.98	0.43	22.69	38.1	1053
16EV017	0.54	43.49	1326	6.17	4.60	0.28	19.98	39.7	1464
16EV070A	0.51	40.72	941	2.52	7.19	0.43	18.42	38.0	1039
16EV070B	0.39	33.59	1294	3.05	4.27	0.26	17.74	33.5	1614
16EV070D	0.55	35.90	1187	5.12	5.18	0.28	19.33	38.0	1377
16EV084	2.13	208.53	2943	9.52	19.43	1.15	46.04	87.4	801
16EV089	2.07	191.76	2547	9.01	19.55	1.12	40.84	83.6	800
16EV099	2.10	190.00	2502	8.76	18.78	1.09	41.13	82.3	821
16EV101	1.97	207.30	2500	9.84	18.87	1.17	41.79	84.6	729
Sample ID	Nd	Zr	Hf	Sm	Eu	Ti	Dy	Yb	Lu
16EV013	20.41	76.1	2.75	4.2	1.86	5149	3.76	2.57	0.40
16EV014	27.01	170.0	4.40	6.2	2.70	5350	6.14	3.41	0.53
16EV017	17.98	132.1	4.02	3.4	1.28	2505	1.78	0.86	0.13
16EV070A	20.91	170.5	4.48	4.8	1.70	6976	4.63	2.65	0.41
16EV070B	15.31	103.4	3.08	3.0	1.31	2970	1.97	1.08	0.17
16EV070D	18.29	115.2	3.44	3.4	1.21	4220	1.95	0.97	0.15
16EV084	40.93	115.1	3.67	8.5	3.12	5937	8.47	4.95	0.76
16EV089	35.64	103.1	3.23	7.3	2.48	6630	6.23	3.57	0.55
16EV099	35.70	99.8	3.14	7.4	2.55	6079	6.42	3.70	0.55
16EV101	35.63	103.9	3.24	7.2	2.31	5160	6.04	3.46	0.52

Table 4: Continued

Sample ID	Cs	Rb	Ba	Th	Nb	Ta	La	Ce	Sr
16EV103A	1.88	207.14	2718	9.82	19.76	1.18	42.44	84.6	757
16EV103B	0.56	35.20	1320	3.37	4.58	0.29	16.74	36.4	1460
16EV124	0.27	34.94	1384	3.36	4.89	0.29	17.00	32.3	1538
16EV164	1.87	47.16	1685	2.88	8.71	0.50	43.96	76.5	1269
16EV166	0.32	7.83	597	1.00	5.00	0.27	14.13	30.9	1154
16EV169	1.38	44.78	1808	3.39	10.38	0.57	28.41	49.1	1258
16EV171	0.67	40.27	1385	2.86	7.51	0.55	30.97	49.7	1100
16EV173	0.74	48.78	1271	3.99	20.39	1.08	41.55	92.9	822
16EV176	0.46	32.86	824	2.00	6.45	0.37	17.49	35.7	1075
16EV283	0.21	36.43	1497	3.14	5.59	0.32	17.54	29.0	1329
Sample ID	Nd	Zr	Hf	Sm	Eu	Ti	Dy	Yb	Lu
16EV103A	35.30	117.4	3.61	7.1	2.41	5706	6.24	3.68	0.57
16EV103B	15.80	102.3	3.23	3.1	1.24	2567	2.11	1.17	0.18
16EV124	13.49	119.8	3.52	2.8	1.44	3072	2.07	1.13	0.18
16EV164	80.56	176.1	4.63	19.6	6.69	6790	11.76	4.96	0.69
16EV166	19.60	107.9	2.89	5.0	1.94	9194	5.21	2.89	0.44
16EV169	36.27	155.7	4.29	9.0	3.55	6208	7.69	3.88	0.59
16EV171	40.13	135.0	3.79	9.4	3.65	5408	9.28	4.95	0.76
16EV173	52.76	404.4	10.04	12.9	3.75	17127	13.40	7.54	1.14
16EV176	21.08	159.8	4.23	4.9	1.73	7636	4.57	2.52	0.39
16EV283	13.46	103.4	3.14	2.9	1.53	3524	2.02	1.14	0.18

Sample ID	Cs	Rb	Ba	Th	Nb	Ta	La	Ce	Sr
16EV284	0.23	33.49	1211	2.73	4.44	0.27	14.92	26.1	1253
16EV286	0.21	26.13	767	1.84	6.03	0.35	16.33	34.1	1108
16EV287	0.48	33.87	1178	5.87	4.47	0.26	19.84	39.7	1740
16EV288	0.77	39.91	1399	6.17	6.66	0.37	30.12	62.9	1561
16EV291A	0.98	113.04	1878	6.74	18.51	1.05	38.98	87.5	792
16EV291B	0.89	89.02	1995	9.46	20.54	1.19	43.05	95.1	759
AGV1	1.25	67.87	1218	6.351	14.52	0.866	38.19	68.6	661
BVHO-1	0.103	9.520	134	1.225	18.53	1.174	15.40	38.1	399
DNC	68.61	4.50	118	6.351	14.52	0.866	38.19	68.6	661
BCR	0.96	46.61	683	5.790	12.74	0.786	25.46	53.9	335
Kuna Yala	0.24	6.24	123	0.29	9.00	0.07	1.41	3.6	174
Eclogite	1.00	4.40	25	1.72	8.18	0.64	13.98	37.-	16
Altered MORB		0.57	1		2.20		1.66	6.2	81
Sample ID	Nd	Zr	Hf	Sm	Eu	Ti	Dy	Yb	Lu
16EV284	10.78	74.6	2.32	2.2	1.27	2655	1.50	0.82	0.13
16EV286	19.72	144.1	3.91	4.6	1.68	7162	4.28	2.35	0.37
16EV287	18.58	125.3	3.64	3.4	1.35	3312	1.94	0.97	0.15
16EV288	27.68	107.8	3.22	4.9	1.75	4090	2.61	1.28	0.20
16EV291A	42.83	310.9	8.57	9.1	2.75	8926	7.28	3.85	0.59
16EV291B	46.53	507.3	12.97	10.3	2.75	7914	9.27	5.36	0.83
AGV1	32.07	231.5	5.09	5.8	1.658		3.58	1.66	0.25
BVHO-1	24.78	174.6	4.44	6.2	2.053	16300	5.27	1.98	0.28
DNC	5.20	38.0	5.09	5.8	1.658		3.58	1.66	0.25
BCR	26.68	190.3	4.923	6.6	1.957		6.39	3.38	0.50
Kuna Yala	4.43	30.0	0.64	1.0	0.43	1.66	1.16	0.14	4.43
Eclogite	29.59	186.0	5.01	8.2	2.34	9.63	5.90	0.90	29.59
Altered MORB	7.45		2.26	2.7	0.97		4.50	2.81	0.45

APPENDIX D

PARTITION COEFFICIANTS

Table 5: Partition coefficients used in fractional melting and crystallization models, used from the following studies; Dunn & Sen 1994[1], Nandedkar 2016[2], Hauri et al. 1994[3], Foley et al. 2000[4], Hart Dunn, 1993[5], Fujimaki et al. 1984[6], Paster et al. 1974[7], McKenzie & Onions 1991[8], Botazzi et al. 1999[9], Green & Pearson 1987[10].

Melting	Cs	Rb	Ba	Th	Nb	Ta	La	Ce	Sr
Plagioclase		0.020[1]	0.400[1]	0.000[1]	1.3[1]	1.70[1]	0.10[1]	0.080[1]	1.40[1]
Hornblende		0.330[6]	0.024[2]	0.004[2]	0.058[2]	0.046[2]	0.023[2]	0.028[2]	0.030[2]
Garnet		0.001[8]	0.000[3]	0.009[3]	0.005[3]	0.005[3]	0.001[3]	0.017[3]	0.001[3]
Ilmenite		0.110[4]	0.000[4]	0.000[4]	136.0[4]	8.82[4]	0.098[3]	0.000[4]	0.000[4]
Clinopyroxene		0.001[8]	0.010[5]	0.006	0.005[5]	0.005[5]	0.015[5]	0.038[5]	0.091[5]
Orthopyroxene							0.031[6]	0.221[6]	
Olivine		0.013[1]	0.000	0.000	0.001[1]	0.06[1]	0.001	0.001[1]	0.000
	Nd	Zr	Hf	Sm	Eu	Dy	Yb	Lu	
Plagioclase	0.070[1]	0.000[1]	0.000[1]	0.100[1]	0.050[1]	0.040[1]	0.020[1]	0.010[1]	
Hornblende	0.052[2]	0.017[2]	0.067[2]	0.651[2]	0.124[2]	0.200[2]	0.20[2]	0.20[2]	
Garnet	0.064[3]	0.40[3]	0.40[3]	0.230[3]	1.800[3]	2.000[3]	8.70[3]	7.000[3]	
Ilmenite	0.0001[4]	3.070[4]	4.980[4]	0.000[4]	0.30[4]	0.000[4]	0.000[4]	0.000[4]	
Clinopyroxene	0.167[5]	0.240[5]	0.240[5]	0.253[5]	0.30[5]	0.350[5]	0.43[5]	0.443[5]	
Orthopyroxene	0.221[6]	0.1024[6]	0.015[6]	0.102[6]	1.214[6]	0.050[6]	0.041[6]	0.039[6]	
Olivine	0.0001[1]	0.001[1]	0.001	0.001[1]	0.004[1]	0.008[1]	0.020[1]	0.020[1]	

Table 5: Continued

Crystallization	Cs	Rb	Ba	Th	Nb	Ta	La	Ce	Sr
Plagioclase	0.006[1]	0.020[1]	0.400[1]	0.000[1]	0.000[1]	0.03	0.3926[6]	0.2511[6]	
Hornblende	0.5[10]	0.33[6]	0.024[2]	0.004[2]	0.058[2]	1.000[8]	0.023[2]	0.028[2]	0.030[2]
Quartz									
Ilmenite		0.019[4]	0.014[4]	0.540[4]	2.000	8.820[4]	.237[4]	0.087[4]	0.036[4]
Sphene					3.5[10]	18.9[10]	8.6[10]		
	Nd	Zr	Hf	Sm	Eu	Dy	Yb	Lu	
Plagioclase	0.21[6]	0.0406[6]	0.0391[6]	0.0174[6]	0.21[6]	0.0412[6]	0.1323[6]	0.1384[6]	
Hornblende	0.052[2]	0.017[2]	0.067[2]	0.080[2]	0.124[2]	2.436[8]	0.647[8]	0.604[8]	
Quartz									
Ilmenite	0.277[4]	3.070[4]	4.980	0.150[4]	0.000[4]		0.009[4]	0.012[4]	
Sphene									

REFERENCES

Abratis, M., & Wörner, G. (2001, Feb). Ridge Collision, Slab-window Formation, and the Flux of Pacific Asthenosphere into the Caribbean Realm. *Geology, 29*(2), 127-130.

Bandini, A. N., Flores, K., Baumgartner, P. O., Jackett, S. J., & Denyer, P. (2008). Late Cretaceous and Paleogene radiolaria from the Nicoya peninsula, Costa Rica: a tectonostratigraphic appli- cation . *Stratigraphy, 5*, 3-21.

Barat, F., Mercier de Lépinay, B., Sosson, M., Müller, C., Baumgartner, P. O., & Baumgartner-Mora, C. (2014). Transition from the Farallon Plate subduction to the collision between South and Central America: Gelogical evolution of the Panamá Isthmus. *Tectonophysics, 622*.

Baumgartner, P. O., Flores, K., Bandini, A., Girault, F., & Cruz, D. (2008). Upper Triassic to Cretaceous radiolaria from Nicaragua and northern Costa Rica: the Mesquito composite oceanic terrane. *Ofioliti, 33*, 1-19.

Baumgartner-Mora, C., Baumgartner, P. O., Buchs, D. M., Bandini, A. N., & Flores, K. (2008). Paleocene to Oligocene foraminifera from the Azuero peninsula (Panama): the timing of seamount formation, accretion and forearc overlap, along the Mid-American Margin. *6th Geoscience Meeting, Lugano*, 116-117.

Blakely, R. (1995). Potential Theory in Gravity & Magnetic Applications. *Cambridge University Press*.

Botazzi, P., Tiepolo, M., Vannucci, R., Zanetti, A., Brumm, R., Foley, S. F., & Oberti, R. (1999). Distinct site preferences for heavy and light REE in amphibole and the prediction of Amph/LDREE. *Contributions to Mineralogy and Petrology, 137*, 36-45.

Buchs, D. M., Arculus , R. J., Baumgartner , P. O., Baumgartner-Mora , C., & Ulianov, A. (2010). Late Cretaceous arc development on the SW margin of the Caribbean plate: insights from the Golfito, Costa Rica, and Azuero, Panama, complexes. *Geochemistry, Geophysics, Geosystems, 11*.

Buchs, D. M., Arculus, R. J., Baumgartner, P. O., & Ulianov, A. (2011a). Oceanic intraplate volcanoes exposed: example from seamounts accreted in Panama . *Geology, 39*, 335-338.

Buchs, D. M., Baumgartner, P. O., Baumgartner-Mora, C., Flores, K., & Bandini, A. N. (2011b). Upper Cretaceous to Miocene tectonostratigraphy of the Azuero area (Panama) and the discontinuous accretion and subduction erosion along the Middle American margin. *Tectonophysics, 512*, 31-46.

Cady, J. W. (1980, October). Calculation of gravity and magnetic anomalies of finite-length right polygonal prisms Read More: https://library.seg.org/doi/abs/10.1190/1.1441045. *U.S. Geological Survey Bulletin*.

Coates, A. G., Collins, L. S., Aubry, M. P., & Berggren, W. A. (2004). The geology of the Darien, Panama, and the late Miocene–Pliocene collision of the Panama arc with northwestern South America. *Geological Society of America, 116*, 1327-1344.

Corral, I., Gómez-Gras, D., Griera, A., Corbella, M., & Cardellach, E. (2013). Sedimentation and volcanism in the Panamanian Cretaceous intra-oceanic arc and fore-arc: New insights from the Azuero peninsula (SW Panama). *Bulletin de la Société Géologique de France, 184*.

De Boer, J. Z., Defant, M. J., Restrepo, J. F., Clark, L. F., & Ramirez, A. H. (n.d.). Quaternary Calc-Alkaline Volcanism in Western Panamá: Regional Variation and Implication for the Plate Tectonic Framework. *1*(3). Journal of South American Earth Sciences.

de Boer, J. Z., Defant, M. J., Stewart, R. H., Restrepo, J. F., & Clark, L. F. (n.d.). *Quaternary calk-alkaline volcanism in western Panama: Regional variation and implication for plate tectonic framework.* (Vol. 1). Journal of South American Science.

Defant, M. J., Clark, L. F., Stewart, R. H., Drummond, M. S., de Boer, J. Z., Maury, R. C., . . . Restrepo, J. F. (1991). Andesite and dacite genesis via contrasting processes: the geology and geochemistry of El Valle Volcano, Panama. *Contributions to Mineralogy and Petrology, 106*, 309-324.

Defant, M. J., Jackson, T. E., Drummond, M. S., De Boer, J. Z., Bellon, H., Feigenson, M. D., . . . Stewart, R. H. (1992). The geochemistry of young volcanism throughout western Panamá and southeastern Costa-Rica: An overview. *J. Geol. Soc. London, 149*, 569-579.

Defant, M. J., Richerson, P. M., De Boer, J. Z., Maury, R. C., Bellon, H., Feigenson, M. D., . . . Jackson, T. E. (1990). Dacite genesis via both slab melting and differentiation: Petrogenesis of La Yeguada volcanic complex, Panamá. *Journal of Petrology, 32*, 1101-1142.

Dunn, T., & Sen, C. (n.d.). Mineral/Matrix Partition-Coefficients for Ortho-Pyroxene, Plagioclase, and Olivine in Basaltic to Andesitic Systems - a Combined Analytical and Experimental-Study. (733, Ed.) *Geochimica et Cosmochimica Acta, 58*(2), 717.

Ewart, A. (1982). The mineralogy and petrology of Tertiary-Recent orogenic volcanic rocks: with special reference to the andesitic-basaltic compositional range. *Andesites: Orogenic Andesites and Related Rocks 7* , 25-98.

Farris, D. W., Bayona, G., Restrepo-Moreno, S. A., Montes, C., Cardona, A., Mora, A., . . . Valencia, V. (2011). Fracturing of the Panamanian Isthmus During Initial Collision with South America. *Geology, 39.11*, 1007-1010.

Farris, D. W., Cardona, A., Camilo, M., Foster, D., & Jaramillo, C. (2017). Magmatic evolution of Panama Canal volcanic rocks: A record of arc processes and tectonic change. *PLoS One*.

Foley, S. F., Barth, M. G., & Jenner, G. A. (2000). Rutile/melt partition coefficients for trace elements and an assessment of the influence of rutile on the trace element characteristics of subduction zone magmas. *Geochimica et Cosmochimica Acta, 64*(5), 933-938.

Fowler, G. D. (2015). GEOLOGY AND GEOCHEMISTRY OF THE WESTERN PANAMÁ CANAL BASIN VOLCANIC ARC ROCKS.

Fowler, G. D., & Farris, D. W. (2017). Mantle influences on Miocene magmatism in central Panama. *Geological Society of America.* Seattle: GSA.

Fujimaki, H., Tatsumoto, M., & Aoki, K. (1984). Partition coefficients of Hf, Zr, and REE between phenocrysts and groundmasses. *Journal of Geophysical Research , 89*, 662-672.

Gerya, T. V., Stern, R. J., Baes, M., Sobolev, S. V., & Whattam, S. A. (2015). *Plate tectonics on the Earth triggered by plume-induced subduction initiation* (Vol. 527). Nature.

Goff, J., & Cochran, J. (1996). *The Bauer scarp ridge jump, a complex of tectonic sequence revealed in satellite altimetry.* (Vol. 141). Earth Planet Sciene.

Goss, A. R., & Kay, S. M. (2006). Steep REE Patterns and Enriched Pb Isotopes in Southern Central American Arc Magmas: Evidence for Forearc Subduction Erosion. *Geochemistry, Geophysics, Geosystems, 7*.

GRASS Development Team, 2017. (n.d.). Geographic Resources Analysis Suppory System (GRASS) Software, Version 7.2.1. Open Source Geospatial Foundation. https://grass.osgeo.org.

Green, T. H., & Pearson, N. J. (1987). An expeirimental study of Nb & Ta partitioning between Ti-rich minerals and silicate liquids at high pressure and temperature. *Geochimica and Cosmochemica Acta., 51*.

Hart, S. R., & Dunn, T. (1993). Experimental cpx/melt partitioning of 24 trace elements. *Contributions to Mineralogy and Petrology, 113*, 1-8.

Hauri, E. H., Wagner, T. P., & Grove, T. L. (1994). Experimental and natural partitioning of Th, U, Pb and other trace elements between garnet, clinopyroxene and basaltic melts. *Chemical Geology, 117*, 149-166.

Hidalgo, P. J., Vogel, T. A., Rooney, T. O., Currier, R. M., & Layer, P. W. (2011). Origin of Silicic Volcanism in the Panamanian Arc: Evidence for a Two-stage Fractionation Process at El Valle Volcano. *Contributions to Mineralogy and Petrology, 162*(6), 1115-1138.

Klein, E. M. (2003). Geochemistry of the igneous oceanic crust. Treatise on Geochemistry. Elsevier. 433-463.

Le Bas, M. J., Le Maitre, R. W., Streckeisen, A., & Zanettin, B. (1986). A chemical classification of volcanic rocks based on the total alkali-silica diagram. *Journal of Petrology, 27*(3), 745-750.

Lissinna, B. (2005). A Profile Through the Central American Landbridge in Western Panama: 115 Ma Interplay Between the Galápagos Hotspot and the Central American Subduction Zone. *Methemtaisch-Naturwissenschftlichen Fakultät* , 102.

Lonsdale, P. (2005, June 27). Creation of the Cocos and Nazca plates by fission of the Farallon plate. *Tectonophysics*. La Jolla, CA, USA: Science Direct.

McDonough, W. F., & Sun, S. (1995). The Composition of the Earth. *Chemical Geology*, 223-254.

McKenzie, D., & O'Nions, R. K. (1991). Partial melt distributions from inversion of rare Earth element concentrations. *Journal of Petrology, 32*, 1021-1091.

Meschede, M., & Frisch, W. (1998). A plate tectonic model for the Mesozoic and early Cenozoic history of the Caribbean plate. *Tectonophysics, 296*.

Montes, C., Bayona, G., Cardona, A., Buchs, D. M., Silva, C. A., Moron, S., . . . Valencia, V. (2012). Arc-Continent Collision and Orocline Formation: Closing of the Central America Seaway. *Journal of Geophysical Research , 117*.

Montes, C., Cardona, A., McFadden, R., Morón, S. E., Silva, C. A., Restrepo-Moreno, S., . . . Flores, J. A. (2012b). Evidence for middle Eocene younger land emergence in central Panamá: Implications for Isthmus closure. *GSA Bulletin, 124*, 790-799.

Mora, A. (2010). Tectonic history of the Andes and sub-Andean zones: implications for the development of the Amazon drainage basin: Amazonia, Landscape and Species Evolution: A Look into the Past. *Blackwell Publishing*.

Nandedkar, R. H., Hurlimann, N., Ulmer, P., & Müntener, O. (2016). Amphibole–melt trace element partitioning of fractionating calc-alkaline magmas in the lower crust: an experimental study. *Contributions to Mineralogy and Petrology, 171*(8-9).

Paster, T. P., Schauwecker, D. S., & Haskin, L. A. (1974). The behavior of some trace elements during solidification of the Skaergaard layered series. *Geochimica et Cosmochimica Acta, 38*(10), 1549-1577.

Peacock, S. M., Rushmer, T., & Thompson, A. B. (1994). Partial melting of subducting oceanic crust. *Earth and Planetary Science Letters, 121*.

Pearce, J. A., & Peate, D. W. (1995). Tectonic implications of the composition of volcanic arc magmas. *Annual Review of Earth and Planetary Sciences, 23*.

Ridolfi, F., Renzulli, A., & Puerini, M. (2010). Stability and chemical equilibrium of amphibole in calc-alkaline magmas: an overview, new thermobarometric formulations and application to subduc- tion-related volcanoes. *Contributions to Mineralology and Petrology, 160*.

Rooney, T. O., Morell, K. D., Hidalgo, P., & Fraceschi, P. (2015). Magmatic consequences of the transition from othogonal to oblique subduction in Panama. *Geochemistry, Geophysics, Geosystems, 16*, 4178-4208.

Sandwell, D. T., & Smith, W. H. (2009). Global marine gravity from retracked Geosat and ERS-1 altimetry: Ridge segmentation versus spreading rate. *Journal of Geophysical Research, 114*.

Sempere, T., Herail, G., & Bonhomme, M. (1990). *Late Oligocene-early Miocene major tectonic crisis and related basins in Bolivia.* (Vol. 18). Geology.

Silver, E. A., Reed, D. L., Tagudin, J. E., & Heil, D. J. (n.d.). *Implications of the north and south Panama thrust belts for the origin of the Panama orocline* (Vol. 9). Tectonics.

Stracke, A., Bizimis, M., & Salters, J. M. (2003, March 5). Recycling Oceanic Crust: Quantitative Constraints. *Geochemistry, Geophysics, Geosystems, 4*(3).

Talwani, M., & M., E. (1959). Rapid computation of gravitational attraction for two-dimensional bodies with application to the Mendocino submarine fracture zone. *J. Geophysics Res., 64*.

Trankamp, R., Kellogg, J. N., Freymueller, J. T., & Mora, H. P. (2002). Wide plate margin deformation, southern Central America and northwestern South America, CASA GPS observations. *Journal of South American Earth Sciences, 15*, 157-171.

Wegner, W., Wörner, G., Harmon, R. S., & Jicha, B. R. (2011). Magmatic history and evolution of the Central American Land Bridge in Panama since Cretaceous times. *Geology, 123*, 703-724.

Whattam, S. A., Montes, C., McFadden, R. R., Cardona, A., Ramirez, & Valencia, V. (2012). Age and origin of the earliest adakitic-like magmatism in Panamá: Implications for the tectonic evolution of the Panamánian magmatic arc system. *Lithos, 142-143*.

Zhang, G., Song, S., Zhang, L., & Niu, Y. (2008). The subducted oceanic crust within continental-type UHP metamorphic belt in the North Qaidam, NW China: Evidence from petrology, geochemistry and geochronology. *Lithos*.

BIOGRAPHICAL SKETCH

Keith Richard Munsey was born to Martin and Margaret Munsey in Plantation, Florida on December 3rd of 1990. After graduating from Lincoln High School in 2009, Keith began his college career at Tallahassee Community College before transferring to Florida State University. In December of 2014 he graduated with his Bachelor of Science in Geology with a minor in Environmental Science. After taking a semester off, Keith begin his Master's degree within Florida State University's Department of Earth Ocean and Atmospheric Sciences, pursuing an advanced degree in Geology, with an emphasis in geochemistry and geophysics. In his time at Florida State University he has been a part of numerous national academic organizations and held an internship at the Florida Geological Survey.